

An Error Model for Biomass Estimates Derived From Polarimetric Radar Backscatter

Scott Hensley, *Senior Member, IEEE*, Shadi Oveisgharan, Sassan Saatchi, *Member, IEEE*,
Marc Simard, Razi Ahmed, *Member, IEEE*, and Ziad Haddad

Abstract—Estimating the amount of above ground biomass in forested areas and the measurement of carbon flux through the quantification of disturbance and regrowth are critical to develop a better understanding of ecosystem processes. Well-resolved and globally consistent inventories of forest carbon must rely on remote sensing measurements, particularly from polarimetric radars. While a wide variety of studies conducted over the past three decades have shown how radar polarimetric measurements can be used to estimate above ground carbon for regions with less than 100 Mg of biomass per hectare, there is no established methodology for assessing biomass estimation accuracy based on *a priori* instrument and mission parameters. In this paper, a framework for assessing biomass estimation accuracy is presented that is a blend of the basic imaging physics and empirically derived parameters that describe various relationships between biomass and radar polarimetric observable quantities. The implications of this error model on the design and performance of a polarimetric radar are explored using instrument, mission, and science parameters from a notional Earth observing mission.

Index Terms—Backscatter error model, forest biomass, polarimetry, synthetic aperture radar (SAR).

I. INTRODUCTION

THE need to better understand climate change and ecosystem processes coupled with recent advances in remote sensing techniques such as radar and lidar has precipitated the push for the global accounting of carbon storage, flux, and land-use change [1]. Several measurement paradigms have been suggested for making such measurements, including polarimetric radars operating at L- or P-bands, using a combination of lidar and polarimetric radar measurements [2], or through polarimetric–interferometric observations such as the proposed Tandem-L mission [3]. Polarimetric radars have been successfully used for estimating biomass with a spatial resolution of 100 m for regions with biomass values ranging from 50 to 300 Mg/ha above which inversion is complicated by issues of signal saturation [4]. Various studies [5]–[7] have demonstrated the relationship between polarimetric radar measurements and forest biomass in different ecoregions and biomes by relating backscatter measurements to field data coupled with some scattering models, for instance, using shuttle imaging radar A (SIR-A) data over a pine plantation in Alabama [8], airborne

synthetic aperture radar (AIRSAR) data over the Landes pine forest in southwest France [9], or shuttle imaging radar C (SIR-C) data over Raco, Michigan [10], among others.

Such studies have invariably focused on small regions where field measurements of biomass can be made; consequently, no consistent repository of radar-derived global forest biomass exists. A critical component of the several proposed spaceborne missions for measuring biomass, including European Space Agency (ESA)’s proposed Biomass mission [11] and National Aeronautics and Space Administration (NASA)’s proposed L-band radar mission [2], [12], is the development of such a data set using polarimetric radar. Unfortunately, there is no established framework for *a priori* assessing the biomass estimation accuracy for such systems that is critical for insuring proper instrument and mission design to meet mission requirements. Here, we describe such a framework in the form of an error model that is immediately applicable to the aforementioned proposed missions but generic enough to be useful elsewhere. It is expected that this first generation model will evolve as more data are examined and compared with the model predictions. In addition, more sophisticated error modeling approaches, i.e., Bayesian methods, that are also amenable to implementation for both estimating biomass and quantifying estimation are possible but not described herein.

The organization of this paper is as follows. Section II describes the functional form used in this paper for relating radar backscatter and forest biomass. Section III lays out the mathematical framework for the backscatter error model with explanations of each contributing term. In Section IV, we discuss how to use the backscatter error model to estimate uncertainty in biomass estimates. Section V develops the formula for the minimum dimensions of a cell size needed to achieve specific biomass estimation accuracy. In Section VI, we propose a definition of saturation that depends on the desired biomass estimation accuracy and hence represents a more functional definition on the usable range of biomass for which the desired estimation accuracy is possible. Section VII summarizes the data-driven aspects of the model and highlights where additional measurements are needed, while Section VIII uses a notional L-band spaceborne radar patterned after the proposed NASA L-band instrument, mission, and science parameters as an example to illustrate this error model.

II. BIOMASS AND POLARIMETRIC BACKSCATTER RELATIONSHIPS

Radars do not measure forest biomass directly; however, radar backscatter is sensitive to structural attributes of forests.

Manuscript received December 20, 2012; revised June 11, 2013; accepted August 4, 2013. Date of publication September 23, 2013; date of current version February 27, 2014. This research was conducted at the Jet Propulsion Laboratory, California Institute of Technology, under contract with the National Aeronautics and Space Administration.

The authors are with the Jet Propulsion Laboratory, California Institute of Technology, Pasadena, CA 91109 USA (e-mail: shelsy@jpl.nasa.gov).

Digital Object Identifier 10.1109/TGRS.2013.2279400

TABLE I
FIT PARAMETERS FOR σ AS FUNCTION OF BIOMASS FOR $\alpha = 1.0$

Parameter	HH	VV	HV
A	.2295	0.1675	0.0620
B	0.0408	0.0248	0.0328
C	.0001	-9.8923×10^{-6}	-0.0004

TABLE II
FIT PARAMETERS FOR σ AS FUNCTION OF BIOMASS FOR $\alpha = 0.2$

Parameter	HH	VV	HV
A	0.250	0.068	0.190
B	0.007	0.006	0.005
C	0.070	0.018	0.040

This sensitivity leads to the apparent relationship between radar backscatter and biomass that is often observed when radar measurements are compared with biomass estimates derived from *in situ* data. Many functional forms for relating backscatter to biomass, or conversely, have been implemented in the literature some of which are purely mathematically convenient while some are based on semi-empirical scattering models. Although the exact form of the relationship is not integral to the discussion here, any model chosen for analysis should satisfy two basic criteria. First, that it should accurately reflect the mean observable backscatter levels as a function of biomass independent of the sensor used to derive the fits. Ideally, the data used in the fits should encompass the full range of imaging and environmental conditions over which the backscatter data will be employed for biomass estimation, including incidence angle range, weather and/or seasonal variations, biome, and terrain types. Second, as the model is very sensitive to the derivative of biomass with respect to backscatter, it is necessary to take care that the derivative is well reflected by the model parameters.

For this paper, the polarimetric backscatter measurements, σ_{hh} , σ_{hv} , and σ_{vv} , were related to biomass b using the following functional form based on the distorted Born approximation:

$$\sigma(b) = f_{veg} (A_{pq}(1 - e^{-B_{pq}b}) + C_{pq}b^{\alpha}e^{-B_{pq}b}) + (1 - f_{veg})\sigma_{bare} \quad (1)$$

where f_{veg} is the fraction of a cell that is vegetated (assumed unity throughout this paper), A_{pq} , C_{pq} , B_{pq} , ($pq = hh, hv, vv$), and α are fit coefficients, and σ_{bare} is the backscatter from bare surfaces. Tables I and II give the fit parameters for backscatter as a function of biomass for $\alpha = 1.0$ and $\alpha = 0.2$, while Fig. 1 shows plots of the fits of backscatter as a function of biomass for the HH, HV, and VV polarizations for cases $\alpha = 1.0$ and $\alpha = 0.2$.

Whether using multiple polarizations offers an advantage to biomass estimation depends on the amount of additional information contained in each polarimetric channel. That is to say, if the channels are perfectly correlated, there is no new information to be gained by using an additional polarimetric observation, and conversely combining uncorrelated polarimetric observations sensitive to biomass may help improve the quality of backscatter-derived biomass estimates. The uncertainty of biomass estimates using polarimetric radar measurements depends on two major factors, the sensitivity of the backscatter

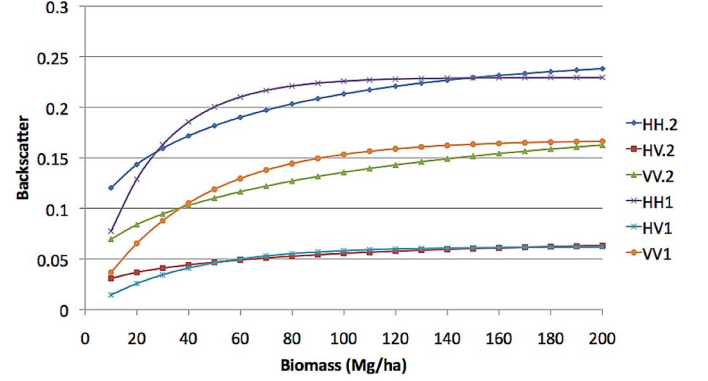


Fig. 1. Plot of σ as a function of biomass in Mg/ha for the HH, HV, and VV polarizations. Note how σ tends to saturate around 100 Mg/ha, leading to large $\partial b / \partial \sigma$ derivatives.

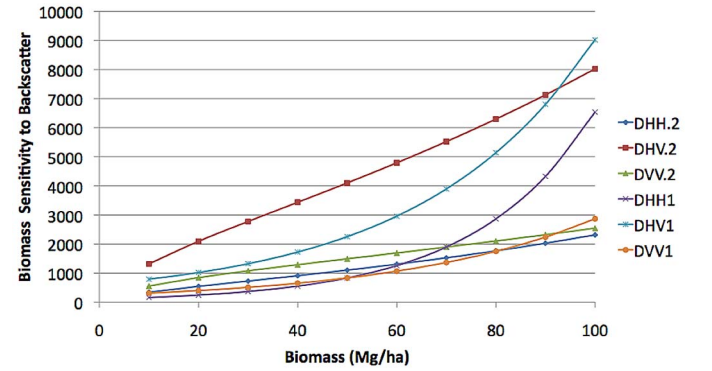


Fig. 2. Plots of $\partial b / \partial \sigma$ as a function of biomass for HH, HV, and VV polarizations for the $\alpha = 0.2$ and $\alpha = 1.0$ cases. Units for the vertical axis are backscatter (m^2/m^2) per unit biomass (Mg/ha), resulting in units of ha/Mg .

biomass relationship and the error in backscatter measurements themselves. The sensitivity is given by the derivative of the model (1) with respect to biomass

$$\frac{\partial \sigma}{\partial b}(b) = f_{veg} [B_{pq}(A_{pq} - C_{pq}b^{\alpha pq}) + C_{pq}\alpha pq b^{\alpha pq - 1}] e^{-B_{pq}b}. \quad (2)$$

As this derivative approaches zero, the backscatter measurements show no sensitivity to biomass, leading to large uncertainties. Fig. 2 shows the derivatives of biomass with respect to backscatter, the inverse of (2), plotted as a function of biomass for the coefficients listed in Tables I and II.

The second major factor in determining the uncertainty in radar-derived backscatter estimates is the error in backscatter measurements. The following section lays the foundational framework for determining the expected error in polarimetric radar data.

III. MODELING ERROR SOURCES IN RADAR BACKSCATTER

Here, we describe a model of expected error in polarimetric backscatter measurements based on various instrument and imaging parameters with a detailed account of each

contributing error source. The errors in polarimetric backscatter values $\Delta\sigma_{pq}$, ($pq = hh, hv, vv$), are given by

$$\Delta\sigma_{pq} = \left[\left(\frac{1}{\sqrt{N}} \frac{1}{\sqrt{N_{os}}} + \frac{1}{\sqrt{N}} \frac{1}{\sqrt{N_{ot}}} \frac{1 + \frac{\text{SNR}}{\text{MNR}}}{\text{SNR}} \right) \sigma_{pq} + \frac{1}{\sqrt{N_{ot}}} \Delta\sigma_{pq_t} + \frac{1}{\sqrt{N_{ot}}} \Delta\sigma_c + \sqrt{\frac{A_{dem}}{A_{pix}}} \frac{1}{\sqrt{N}} \frac{1}{\sqrt{N_{os}}} \Delta\sigma_a \right] \quad (3)$$

where N is the number of spatial looks, i.e., the number of contiguous radar image pixels averaged together within a biomass estimation cell [see illustration in Fig. 7 and explicit formulation in (25)], $N_{ot} = N_{os} + N_{oi}$ is the sum of the number of speckle identical observations N_{oi} and speckle diverse observations N_{os} , SNR is the thermal signal-to-noise ratio, MNR is the multiplicative noise ratio (a function of the ambiguities, quantization noise, and integrated sidelobe ratios; see Section III-A), A_{dem} and A_{pix} are the areas of the digital elevation model (DEM) pixels and single-look-complex image pixels, respectively, $\Delta\sigma_{pq_t}$ is the temporal variability of the backscatter commensurate to the biomass estimation cell size, $\Delta\sigma_a$ is the error in the backscatter from incorrect area projection normalization, and $\Delta\sigma_c$ is the error in the backscatter calibration. The calibration error term is meant to cover errors associated with the conversion of the raw signal data into calibrated σ_o values except for the area projection term which is book kept separately. In (3), observations are divided into two classes, speckle identical and speckle diverse observations. Speckle identical observations are observations for which speckle is highly correlated, such as repeat measurements from similar viewing geometries. Speckle diverse observations, on the other hand, are observations from imaging geometries that are varied enough so that speckle will not correlate, e.g., opposite direction imaging from ascending and descending orbits. Observations sufficiently separated in time such that the speckle has decorrelated can also be considered speckle diverse observations. This time interval needed for speckle to decorrelate is vegetation type dependent; however, 6–12 months are representative values for L-band.

By observing that some of these errors are likely to be uncorrelated, in practice, it is possible to use the rms of these error sources, resulting in improved predicted performance values. In this paper, we elect to use the more conservative approach of summing the error; however, obvious modifications to the formulas in this paper can be used if the rms error model is preferred.

A. Speckle, Thermal, and Multiplicative Noise

The first two terms in (3) come from the well-known *kpc* equation in radar scatterometry [13] which relates the relative backscatter error to the number of looks and SNR by

$$\begin{aligned} \frac{\Delta\sigma}{\sigma} &= \frac{1}{\sqrt{N}} \left(1 + \frac{1}{\text{SNR}} \right) \\ &= \frac{1}{\sqrt{N}} \left(1 + \frac{2}{\text{SNR}} + \frac{1}{\text{SNR}^2} \right)^{\frac{1}{2}}. \end{aligned} \quad (4)$$

This equation is derived by assuming complex Gaussian-distributed radar data that, after detection, are exponentially distributed, and while it takes into account thermal noise, it does not consider multiplicative noise sources such as ambiguities, impulse response sidelobes, and quantization noise. To account for multiplicative noise, we define the effective SNR, $\widetilde{\text{SNR}}$, as the ratio of the signal to total noise n_t which can be expressed as

$$\begin{aligned} \frac{1}{\widetilde{\text{SNR}}} &= \frac{n_t}{s} = \frac{n_T + \frac{s}{\text{MNR}}}{s} \\ &= \frac{1}{\text{SNR}} + \frac{1}{\text{MNR}} = \frac{1 + \frac{\text{SNR}}{\text{MNR}}}{\text{SNR}} \end{aligned} \quad (5)$$

where n_T is the thermal noise and MNR is the multiplicative noise ratio given by

$$\text{MNR}^{-1} = \text{ISLR}_\rho + \text{ISLR}_{az} + \frac{1}{\text{AMB}_t} + \frac{1}{\text{QNR}} \quad (6)$$

where ISLR_ρ and ISLR_{az} are the integrated sidelobe ratios in range and azimuth, AMB_t is the total signal-to-ambiguity ratio (i.e., includes both range and azimuth ambiguities), and QNR is the quantization-to-noise ratio.

Substituting (5) into (4), one obtains the modified *kpc* equation

$$\frac{\Delta\sigma}{\sigma} = \frac{1}{\sqrt{N}} \left(1 + \frac{1 + \frac{\text{SNR}}{\text{MNR}}}{\text{SNR}} \right). \quad (7)$$

Note that, in the limit as MNR goes to infinity, (7) reverts to the classical *kpc* equation, whereas in the limit as SNR goes to infinity, the modified *kpc* becomes

$$\frac{\Delta\sigma}{\sigma} = \frac{1}{\sqrt{N}} \left(1 + \frac{1}{\text{MNR}} \right). \quad (8)$$

The SNR for each polarimetric channel is computed from the backscatter value σ_{pq} , ($pq = hh, hv, vv$), and the system noise equivalent backscattering coefficient $\bar{\sigma}_o$ is computed by

$$\text{SNR}_{pq} = \frac{\sigma_{pq}}{\bar{\sigma}_o} \quad (9)$$

where all quantities in the above equation are in linear units.

We conclude this section with a slight digression that will prove relevant to the material in Section V. Given the number of looks and the relative backscatter error $\Delta\sigma/\sigma$, (4) can be inverted to solve for the SNR to give

$$\text{SNR} = \frac{1 + \sqrt{N} \frac{\Delta\sigma}{\sigma}}{\left(N \left(\frac{\Delta\sigma}{\sigma} \right)^2 - 1 \right)} = \frac{1}{\sqrt{N} \frac{\Delta\sigma}{\sigma} - 1}. \quad (10)$$

It is useful to point out implications of (10). Taking the limit as $\Delta\sigma$ goes to zero yields

$$\lim_{\Delta\sigma \rightarrow 0} \text{SNR} \rightarrow -1. \quad (11)$$

This limit is problematic as it leads to a nonsensical negative SNR. The reason for this is simply that a certain number of looks are necessary to beat down speckle noise even if there

is infinite SNR. Forcing the denominator in (10) to be positive yields the following inequalities:

$$\Delta\sigma \geq \frac{\sigma}{\sqrt{N}} \quad \text{or} \quad N \geq \left(\frac{\sigma}{\Delta\sigma}\right)^2. \quad (12)$$

Thus, in order to have a nonnegative SNR, one of the following conditions must hold.

- 1) The required radiometric allowable rms error must be larger than the backscatter value divided by the square root of the number of looks.
- 2) The number of looks must exceed the backscatter value divided by the desired radiometric accuracy quantity squared.

A generalization of the inequality in (12) will be used to derive a minimal area constraint on biomass estimation in Section V.

1) *MNR Terms*: This section will provide a brief summary of the terms needed to estimate the MNR as given by (6).

Quantization-to-noise ratio: The quantization-to-noise ratio QNR (expressed in decibels) is defined as the ratio of the signal power to quantization noise power, and it can be approximated by

$$\begin{aligned} \text{QNR} &= 10 \log_{10} \left(\frac{P_{max}}{N_b} \right) = 10 \log_{10} \left(\frac{3 \cdot 2^{2b_q}}{2} \right) \\ &= 10 \log_{10} \left(\frac{3}{2} \right) + 20 \log_{10}(2) b_q \\ &\approx 2.0 + 6.02 b_q \end{aligned} \quad (13)$$

where b_q is the number of bits in the analog to digital converter.

Integrated sidelobe ratio (ISLR): As the ISLR terms in the error model are a function of the range and azimuth weighting functions, an expanded exposition is given for these terms. The primary factor affecting the ISLR term is the radar impulse response functions in range and azimuth. The impulse response depends on the spectral weighting used to control impulse response function sidelobes in range and azimuth. Many weighting functions are possible, e.g., cosine-on-pedestal (which includes Hanning and Hamming weights), Taylor, and Kaiser, as well numerous others. For the purposes of performance analysis, the cosine-on-pedestal weighting will be used which, by adjusting the height of the pedestal, supports a variety of weighting options. Moreover, a closed-form expression of the impulse response function is possible in this case.

The cosine-on-pedestal weighting function $c_p(f, \eta)$ is given by

$$c_p(f, \eta) = \frac{1 + \eta}{2} + \frac{1 - \eta}{2} \cos \left(\frac{2\pi f}{B} \right) \quad (14)$$

where $B/2 \leq f \leq B/2$ and $0 \leq \eta \leq 1$. Several values of η are noteworthy, namely, $\eta = 1$ corresponds to uniform weighting, the typical sinc impulse response, $\eta = 0$, corresponds to Hanning weighting, and $\eta = 0.08$ corresponds to Hamming

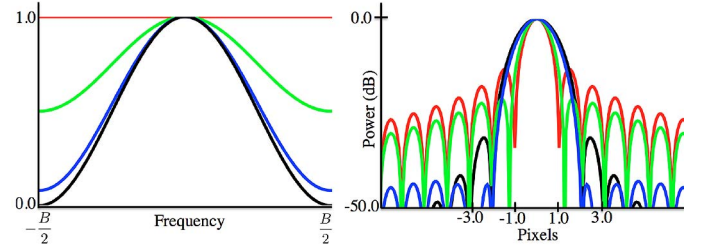


Fig. 3. Weighting functions shown (on the left) with associated impulse response functions (on the right) for various values of η . The red curves show a uniform weighting ($\eta = 1.0$), green curves are for $\eta = 0.5$, blue curves are a Hamming weighting of $\eta = 0.08$, and black curves are a Hann weighting for $\eta = 0.0$.

weighting as illustrated in Fig. 3. The impulse response $I(x)$ with a cosine-on-pedestal weighting function is given by

$$\begin{aligned} I(x) &= \frac{2}{B(1 + \eta)} \int_{-\frac{B}{2}}^{\frac{B}{2}} e^{-\frac{4\pi i f x}{c}} \\ &\quad \times \left[\frac{1 + \eta}{2} + \left(\frac{1 - \eta}{2} \right) \cos \left(\frac{2\pi f}{B} \right) \right] df. \end{aligned} \quad (15)$$

This integral can be carried out in closed form to give

$$\begin{aligned} \tilde{I}(x) &= |I(x)|^2 = \left[\text{sinc} \left(\frac{\pi x}{\Delta x} \right) \right. \\ &\quad \left. + \frac{1}{\pi} \frac{1 - \eta}{1 + \eta} \sin \left(\frac{\pi x}{\Delta x} \right) \left(\frac{\frac{x}{\Delta x}}{1 - \left(\frac{x}{\Delta x} \right)^2} \right) \right]^2 \end{aligned} \quad (16)$$

where we have used the relationship $\Delta x = c/2B$ and have normalized the impulse response so that it has a peak value of 1. Fig. 3 shows weighting functions with associated impulse responses for the same noteworthy values of η discussed previously.

The ISLR is a measure of the ratio of the energy in the sidelobes to the amount of energy in the main lobe. The edge of the main lobe is defined to be the location of the null of the first sidelobe of the ideal impulse response with whatever nominal weighting assumed. The sidelobe region is, by definition, the region from outside the null of the first sidelobe of the ideal impulse response to k times the main-lobe width. Letting $\tilde{I}(x)$ be the impulse response function with the peak assumed to be located at $x = 0$ and the location of the first null at κ_η , then the ISLR¹ is given by

$$\text{ISLR} = \frac{\int_{-\kappa_\eta}^{\kappa_\eta} \tilde{I}(x) dx + \int_{\kappa_\eta}^{k\kappa_\eta} \tilde{I}(x) dx}{\int_{-\kappa_\eta}^{\kappa_\eta} \tilde{I}(x) dx}. \quad (17)$$

¹Note that the ISLR multiplicative noise term is defined in an inverse fashion to the ambiguity and quantization noise terms. This definition facilitates quantifying the increase in ISLR from random phase variations, but it means that it has a reciprocal relationship compared with the other noise terms.

In order to compute the integrals in (17), it is necessary to know the location of the null of the first sidelobe, κ_η . By rewriting the function $\tilde{I}(x)$ as

$$\begin{aligned}\tilde{I}(x) &= \sin\left(\frac{\pi x}{\Delta x}\right) \left[\frac{\Delta x}{\pi x} + \frac{1}{\pi} \frac{1-\eta}{1+\eta} \frac{x}{1 - \left(\frac{x}{\Delta x}\right)^2} \right] \\ &= \sin\left(\frac{\pi x}{\Delta x}\right) g(x)\end{aligned}\quad (18)$$

it is clear that the zeros of $\tilde{I}(x)$ occur where either $\sin(\pi x/\Delta x)$ has a zero or $g(x)$ has a zero. Note at $x = \Delta x$ that $\sin(\pi x/\Delta x)$ is zero and $g(x)$ is indeterminate which leads to the broadening of the main lobe. Of course, $\sin(\pi x/\Delta x)$ has zeros at $x = n\Delta x$, and $g(x)$ has a zero at $x = \Delta x \sqrt{(1+\eta)/2\eta}$. When the zero of $g(x)$ exceeds $2\Delta x$ which occurs for $\eta = 1/7$, then the null of the main lobe achieves its maximal broadening since, at that point, the impulse function gets a zero from the sin term. Hence, the null of the first sidelobe is given by

$$\kappa_\eta = \begin{cases} 3\Delta x & 0 \leq \eta \leq \frac{1}{7} \\ 2\Delta x & \frac{1}{7} < \eta \leq 1. \end{cases}\quad (19)$$

As η varies, so does the effective resolution. The main-lobe broadening factor k_{b_η} which is the inverse ratio of the width of the main lobe with uniform weighting ($\eta = 1$) to the width of the main lobe with tapered weighting is given by

$$k_{b_\eta} = \min \left\{ \sqrt{\frac{1+\eta}{2\eta}}, 2 \right\}\quad (20)$$

if the broadening is defined in terms of the null width. Other definitions are possible, e.g., the width of the main lobe at half power in which case the solution is not possible in closed form. However, the following approximate form:

$$k_{b_\eta} \approx 1.6363 - 0.6363\sqrt{\eta}\quad (21)$$

can be used for the half-power main-lobe width broadening factor.

In general, closed-form expressions for the integrals in (17) are not possible and must be done numerically. A value of $k = 10$ is typical for computing the ISLR. Note that the definition of ISLR selected for the performance analysis insures that formulas for increased ISLR due to effects such as pulse repetition frequency (PRF) jitter are not confused with the slight broadening of the main lobe due to quadratic phase errors that increase the width of the main lobe and blur the location of the null of the first sidelobe as shown in Figs. 4 and 5. For quick analysis, the following cubic polynomial for ISLR as a function of η :

$$\text{ISLR}(\eta) \approx -46.965 + 104.11\eta - 112.59\eta^2 + 43.124\eta^3\quad (22)$$

is sufficient and is the implementation employed in this paper.

Ambiguities: Range and azimuth ambiguities in synthetic aperture radar (SAR) systems refer to the contamination of the returned echo from a desired resolution element on the surface with the returned echoes from other regions which are ambiguous in both time delay (range) and Doppler frequency (azimuth). Ambiguity in the range dimension arises from the inability to unambiguously associate a reflected pulse with the

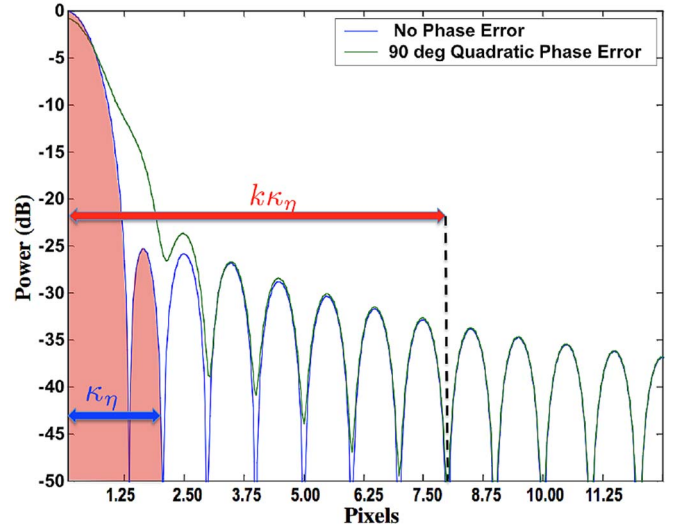


Fig. 4. Figure showing the main-lobe region shaded in red extended to the null of the first sidelobe of the ideal response and the sidelobe region in white extending from the edge of the main lobe out to k_n times the width of the main lobe.

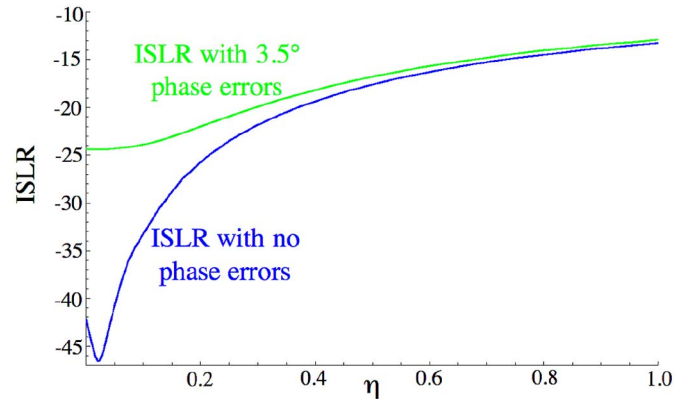


Fig. 5. Plot of the ISLR as a function of η with and without additional random phase noise.

transmitted pulse from which it originated. This ambiguity arises because a reflected pulse with measured time delay τ could be associated to a slant range ρ if it was assumed to have been generated by a transmitted pulse n , or be associated with a slant range $\rho + c/(2\text{PRF})$ if it was assumed to have been generated from pulse $n - 1$ transmitted $\text{PRI} = 1/\text{PRF}$ earlier than pulse n . The ambiguity in the azimuth direction is a result of the discrete sampling of the echoes at the PRF used to extract azimuth information. That is, a reflected train of pulses having a single Doppler frequency component of f_d and a reflected pulse train having a single Doppler component of $f_d + \text{PRF}$ would result in the same set of measurements when sampled at the PRF rate by the Nyquist theorem.

Fortunately, the ambiguous regions do not contribute equally to the amount of energy in a resolution element due primarily to a reduction in gain from the antenna pattern. Thus, the extent to which the ambiguous regions fall in the sidelobe regions of the antenna pattern and how fast the gain of the antenna drops off in the main lobe and within the sidelobes control the amount of ambiguous energy within a resolution element.

Range and azimuth ambiguities are computed based on the imaging geometry, the antenna pattern, and instrument and processing parameters. The signal-to-ambiguity ratio,² AMB, is the ratio of the power returned from the intended image resolution element to the power returned from all the regions ambiguous to the intended image resolution element. Since ambiguities are a rather complicated function of the radar operating parameters and the antenna pattern, explicit formulas are not provided in this paper, however a description of how to compute ambiguities can be found in many sources, e.g., [14].

2) *Spatial Looks*: Spatial looks are obtained by averaging a block of contiguous detected single look, i.e., full resolution, SAR pixels in order to reduce noise. The number of looks depends on the range and azimuth resolutions which are affected by the type of processing done to the data. In particular, the effective range and azimuth resolutions depend on the type of weighting done to the data to reduce impulse response sidelobes as described in Section III-A1.

The range resolution $\Delta\rho$ prior to any range weighting is given by

$$\Delta\rho = \frac{c}{2B} \quad (23)$$

where c is the speed of light and B is the range bandwidth. The azimuth resolution Δs prior to any azimuth weighting is given by

$$\Delta s = \frac{L_{az}}{2} \quad (24)$$

where L_{az} is the antenna azimuth dimension. Letting κ_ρ and κ_s be the range and azimuth impulse response broadening factors given by (21), then, the effective number of spatial looks, N , for estimating biomass is given by

$$N = \frac{\Delta g^2 \sin \theta_i}{\kappa_\rho \Delta \rho \kappa_s \Delta s} \quad (25)$$

where Δg is the desired ground spacing, or cell size, for making the biomass measurement and θ_i is the incidence angle.

Note that there is an implicit assumption in the above computation of the spatial looks, i.e., the area remains homogeneous over the cell size. This assumption will break down at different scales depending on the biome. One of the empirical parameters that must be supplied to the model is the maximal cell size for which spatial averaging reduces the variance before the intrinsic spatial heterogeneity of the vegetation causes the variance to increase.

B. Temporal Variability Errors

The measured backscatter varies from observation to observation due to wind, weather, soil, and vegetation moisture level changes, flooding, or other minor disturbances that are not the result of changes in above ground biomass. The amount of temporal variability depends on biomass estimation cell size, the maximal time interval between observations, biomass level, and biome type. Table III shows measured backscatter

TABLE III
TEMPORAL VARIATION (IN DECIBELS) OBSERVED
IN L-BAND UAVSAR RADAR BACKSCATTER

Site	Biome	Duration	HH	HV	VV
Harvard Forest, Massachusetts	Temperate	10 days	0.56	0.49	0.44
LaSelva, Costa Rica	Tropical	12 days	0.53	0.54	0.52
Quebec, Canada	Boreal	10 days	0.4	0.3	0.3

variability for different forests in the eastern United States, Costa Rica, and Canada. Note that the short time period variations in backscatter are not due to either biomass changes or phenological changes in the vegetation but are induced by environmental changes between observations resulting from a combination of vegetation moisture, soil moisture, or wind-induced changes in the vegetation. These values are likely to be species and biome dependent; however, for the purposes of this paper, we use a value 0.5 dB.

C. Calibration Errors

The calibration error term is meant to cover errors associated with the conversion of the raw signal data into calibrated σ_o values, and it is given by

$$\Delta\sigma_c = \Delta\sigma_{ran} + \Delta\sigma_p + \sqrt{\frac{N_{ot}}{N_{os}}} \sqrt{\frac{A_{dem}}{A_{pix}}} \frac{1}{\sqrt{N}} \Delta\sigma_{geo} \quad (26)$$

where $\Delta\sigma_{ran}$ is the random variation in backscatter due to uncalibrated instrument variations in gain, $\Delta\sigma_p$ is the error in backscatter due to pointing errors, and $\Delta\sigma_{geo}$ is the error in backscatter resulting from geolocation errors (primary contribution is from errors in the DEM). The three different types of errors in (26) have been roughly grouped into the calibration term because they represent either instrument- or processing-induced errors that arise in the process of converting raw ADC signals into calibrated backscatter measurements.³ We now describe each of these in more detail.

1) *Residual Random Calibration Errors*: The random calibration error term σ_{ran} represents random uncompensated backscatter error that results primarily from uncompensated instrument gain that could originate from a variety of sources, e.g., attenuator setting to actual attenuation level table errors, temperature sensor errors that lead to gain compensation errors, and errors in calibration signals used to make gain adjustments.

The random error component $\Delta\sigma_{dB}$ (specified in decibels) represents an error in the ratio of the measured backscatter to the true value and is given by

$$\Delta\sigma_{dB} = 10 \log_{10} \left(\frac{\sigma_m}{\sigma_t} \right) \quad (27)$$

where σ_m is the measured backscatter and σ_t is the true backscatter. To convert the random error into a linear

²AMB is used to denote the signal-to-ambiguity ratio to avoid confusion with the already used acronym SAR.

³Note that the area projection correction term could have been included in this term; however, it is book kept separately.

backscatter error, $\Delta\sigma_{ran}$, note that

$$10^{\frac{\Delta\sigma_{dB}}{10}} = \frac{\sigma_m}{\sigma_t} = \frac{\sigma_t + \Delta\sigma_{ran}}{\sigma_t} = 1 + \frac{\Delta\sigma_{ran}}{\sigma_t} \quad (28)$$

and thus

$$\Delta\sigma_{ran} = \sigma_t \left(10^{\frac{\Delta\sigma_{dB}}{10}} - 1 \right). \quad (29)$$

Multiple observations, either speckle identical or speckle diverse, reduce the random errors by the square root of the number of observations, and hence, the random error term is scaled by the square root of the total number observations in (3).

2) *Antenna Pattern Gain-Induced Errors From Attitude Errors*: The backscattered radar energy is directly proportional to the illuminated area, which changes as a function of the radar pointing geometry and the antenna patterns. Converting the received backscattered signal into a quantity that is useful for biomass estimation requires compensation for the projected area of the radar resolution element on the ground and the gain of the antenna. Antenna gain compensation relies on the accurate knowledge of the antenna pointing and on the geolocation of the radar pixel. Therefore, pointing, geolocation, and area projection errors result from the imperfect compensation of these terms in the observed backscatter σ_o which is given by

$$\sigma_o = \frac{\sigma_t A_t G_t}{A_c G_c} \quad (30)$$

where A_t and G_t are the true gain and area projection terms and A_c and G_c are the applied compensation terms. As will be apparent shortly, it is the relative error in these terms that is relevant for error modeling which somewhat simplifies the error models.

Differentiating (30) yields

$$\begin{aligned} \Delta\sigma_o &= -\frac{\sigma_t A_t G_t}{(A_c G_c)^2} (A_c \Delta G_c + G_c \Delta A_c) \\ &\approx -\sigma_t \left(\frac{\Delta G_c}{G_c} + \frac{\Delta A_c}{A_c} \right) \end{aligned} \quad (31)$$

where the last equation comes from the assumption that the applied compensation terms are approximately equal to the true values. Thus, from (31), errors in the backscatter resulting from gain and area projection errors can be obtained from relative errors in the gain and area projection correction terms as noted previously. Furthermore, since the total antenna gain G is a product of the transmit and receive antenna gains, G_t and G_r , respectively, the relative gain can be expressed as the sum of the relative gains of the transmit and receive gains as shown by

$$\begin{aligned} \Delta G &= G_t \Delta G_r + G_r \Delta G_t \\ \frac{\Delta G}{G} &= \frac{\Delta G_r}{G_r} + \frac{\Delta G_t}{G_t}. \end{aligned} \quad (32)$$

A sinc pattern suffices for approximating the relative gain differences within the main lobe resulting from pointing errors.

Using a sinc approximation, the total gain G can be written as

$$\begin{aligned} G &= G_t G_r \\ &= \left[\frac{\sin(k_{a_t} \theta_a)}{k_{a_t} \theta_a} \frac{\sin(k_{\rho_t} \theta_\rho)}{k_{\rho_t} \theta_\rho} \right]^2 \left[\frac{\sin(k_{a_r} \theta_a)}{k_{a_r} \theta_a} \frac{\sin(k_{\rho_r} \tilde{\theta}_\rho)}{k_{\rho_r} \tilde{\theta}_\rho} \right]^2 \\ &= \left[\frac{\sin(k_{a_t} \theta_a)}{k_{a_t} \theta_a} \right]^4 \left[\frac{\sin(k_{\rho_t} \theta_\rho)}{k_{\rho_t} \theta_\rho} \frac{\sin(k_{\rho_r} \tilde{\theta}_\rho)}{k_{\rho_r} \tilde{\theta}_\rho} \right]^2 \end{aligned} \quad (33)$$

where k_{a_r} and k_{a_t} are functions of the azimuth receive and transmit beamwidths, k_{ρ_r} and k_{ρ_t} are functions of the range (or elevation) receive and transmit beamwidths, θ_a is the angle off boresight in azimuth, θ_ρ is the angle off the elevation boresight of the transmit beam, and $\tilde{\theta}_\rho$ is the angle off the elevation boresight of the receive beam. The second line of (33) follows, assuming that the azimuth beam pattern is identical for transmit and receive. Letting $q \in \{t, r\}$ denote either the transmit or receive beam and x, y denote the azimuth and elevation arguments of the antenna pattern sinc function, then, the relative transmit/receive gain is given by

$$G_q = \left[\frac{\sin(x)}{x} \frac{\sin(y)}{y} \right]^2 \quad (34)$$

and the associated error is

$$\begin{aligned} \Delta G_q &= 2 \left[\frac{\sin(x)}{x} \frac{\sin(y)}{y} \right] \left[\frac{\sin(x)}{x} \frac{y \cos(y) - \sin(y)}{y^2} \Delta y \right. \\ &\quad \left. + \frac{\sin(y)}{y} \frac{x \cos(x) - \sin(x)}{x^2} \Delta x \right] \\ &= 2 G_q \left[\frac{y \cot(y) - 1}{y} \Delta y + \frac{x \cot(x) - 1}{x} \Delta x \right] \\ \frac{\Delta G_q}{G_q} &= 2 \left[\frac{y \cot(y) - 1}{y} \Delta y + \frac{x \cot(x) - 1}{x} \Delta x \right]. \end{aligned} \quad (35)$$

Although not immediately obvious, two applications of L'Hôpital's rule shows that $\lim_{y \rightarrow 0} y \cot(y) - 1/y = 0$ as expected.

Since, for this analysis, a biomass cell could lie anywhere within the antenna pattern, it is easier to just use a swath-averaged error. Substituting $x, y = k_{\rho_q} \theta_\rho, k_{a_q} \theta_a = (\pi/k\theta_{3dB})\theta$ where θ is the appropriate off boresight angle in range or azimuth, θ_{3dB} is the corresponding 3-dB beamwidth, k is a beam shape factor that, for a uniformly weighted array, would nominally be 1/88, and $\Delta\theta$ is the pointing error; then, the swath-averaged relative gain $\overline{\Delta G}/G$ in the elevation direction is given by

$$\begin{aligned} \frac{\overline{\Delta G}}{G} &= \int \frac{\Delta G}{G} \\ &= \frac{4}{\theta_{3dB}} \frac{\pi \Delta \theta}{k \theta_{3dB}} \int_0^{\frac{\theta_{3dB}}{2}} \left[\cot \left(\frac{\pi \theta}{k \theta_{3dB}} \right) - \frac{k \theta_{3dB}}{\pi \theta} \right] d\theta \\ &= \frac{4\pi \Delta \theta}{k \theta_{3dB}^2} \left[\frac{k \theta_{3dB}}{\pi} \ln \left(\sin \left(\frac{\pi \theta}{k \theta_{3dB}} \right) \right) - \frac{k \theta_{3dB}}{\pi} \ln(\theta) \right]_0^{\frac{\theta_{3dB}}{2}} \end{aligned}$$

$$\begin{aligned}
&= \frac{4\Delta\theta}{\theta_{3dB}} \left[\ln \left[\frac{\pi}{k\theta_{3dB}} \frac{\sin\left(\frac{\pi\theta}{k\theta_{3dB}}\right)}{\frac{\pi\theta}{k\theta_{3dB}}} \right] \right]_0^{\frac{\theta_{3dB}}{2}} \\
&= \frac{4\Delta\theta}{\theta_{3dB}} \ln \left[\text{sinc} \left(\frac{\pi}{2k} \right) \right]. \tag{36}
\end{aligned}$$

The azimuth, or along-track relative gain error, acts differently since an imaged point moves through the main lobe of the azimuth beam during a synthetic aperture. Therefore, it is the integral of the gain over the synthetic aperture that is relevant; thus

$$\begin{aligned}
\frac{\overline{\Delta G}}{G} &= \frac{\frac{\partial}{\partial\theta} \int_{-\frac{\theta_{3dB}}{2}}^{\frac{\theta_{3dB}}{2}} \text{sinc}^2 \left(\frac{\pi\theta}{k\theta_{3dB}} \right) d\theta}{\int_{-\frac{\theta_{3dB}}{2}}^{\frac{\theta_{3dB}}{2}} \text{sinc}^2 \left(\frac{\pi\theta}{k\theta_{3dB}} \right) d\theta} \\
&= \frac{\int_{-\frac{\theta_{3dB}}{2}}^{\frac{\theta_{3dB}}{2}} \frac{\partial}{\partial\theta} \text{sinc}^2 \left(\frac{\pi\theta}{k\theta_{3dB}} \right) d\theta}{\int_{-\frac{\theta_{3dB}}{2}}^{\frac{\theta_{3dB}}{2}} \text{sinc}^2 \left(\frac{\pi\theta}{k\theta_{3dB}} \right) d\theta} \\
&\leq \frac{\frac{4\Delta\theta}{\theta_{3dB}} \ln \left[\text{sinc} \left(\frac{\pi}{2k} \right) \right]}{\int_{-\frac{\theta_{3dB}}{2}}^{\frac{\theta_{3dB}}{2}} \text{sinc}^2 \left(\frac{\pi\theta}{k\theta_{3dB}} \right) d\theta} \\
&= \frac{\frac{4\Delta\theta}{\theta_{3dB}} \ln \left[\text{sinc} \left(\frac{\pi}{2k} \right) \right]}{\frac{2\pi}{k\theta_{3dB}} \int_0^{\frac{\pi}{2k}} \text{sinc}^2(x) dx}. \tag{37}
\end{aligned}$$

This error does not vary much in the range direction, and thus, the swath-averaged error may be taken equal to (37). The total error is then the sum of the contributions from the transmit and receive errors in both range and azimuth. These errors are highly correlated over the radar imaging swath because the antenna beam is very board relative to a biomass estimation cell size. Thus, there is no reduction in noise by spatial averaging for this term, and noise reduction results only from multiple observations. Hence, this term is normalized by the square root of the total number of observations in (3).

3) *Geolocation-Induced Errors*: Geolocation-induced errors are errors in the backscatter that occur because a pixel is not geolocated properly which results in a pointing error and, therefore, an incorrect gain compensation. Geolocation errors are primarily due to errors in the DEM used to transform the slant plane radar image into an orthorectified geolocated image which also results in pointing error as shown in Fig. 6. The solid black line represents the true topography, and the dotted line represents the topography in the DEM used to geolocate the data. The solid green line shows the isorange curve corresponding to the target range and its intersection with the actual terrain and DEM topographic surfaces. The angle between the arrowed solid blue line, which represents the actual line-of-sight vector to the target, and the arrowed dotted red line, which represents the geolocated line-of-sight vector, is proportional to the elevation error and inversely proportional to the range. This angle error results in an incorrect gain compensation and, therefore, a backscatter error as discussed in Section III-C2.

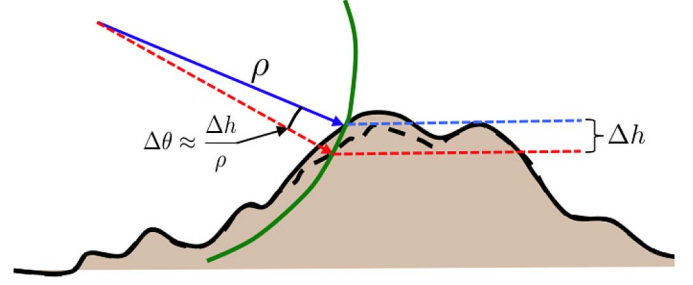


Fig. 6. Illustration of how geolocation errors result in pointing errors. The solid back line represents the true topography, and the dotted line represents the topography in the DEM used to geolocate the data. The solid green line shows the isorange curve corresponding to the target range and its intersection with the actual and DEM topographic surfaces. The angle between the arrowed solid blue line, which represents the actual line-of-sight vector to the target, and the arrowed dotted red line, which represents the geolocated line-of-sight vector, is proportional to the elevation error and inversely proportional to the range.

The geolocation-induced backscatter errors are computed from (36) with the elevation pointing angle error given by

$$\Delta\theta = \frac{\sigma_{h_{dem}}}{\rho} \tag{38}$$

where ρ is the range and $\sigma_{h_{dem}}$ is the height accuracy of the DEM. DEM errors also can result in azimuth angle errors, but these are generally smaller than the elevation angle errors.

Finally, we address the factors multiplying $\Delta\sigma_{geo}$ in (26). For speckle identical observations, as discussed in Section IV, the look geometry is almost identical, and hence, geolocation-induced pointing errors will be nearly the same for these observations. Therefore, geolocation-induced backscatter errors should be reduced by the square root of the number of speckle diverse observations. Since the calibration error term is divided by the square root of the total number of observations in (3), it is multiplied by that quantity and then divided by the square root of the number of speckle diverse observations in (26). If we had a DEM with resolution equal to or better than the radar resolution with independent height error between posts, the geolocation-induced pointing error would be random for each pixel, and the error would go down by the square root of the spatial looks. However, this is not usually the case, and the DEM posting is finer than the biomass estimation cell size but greater than the radar pixel size as illustrated in Fig. 7. This results in the geolocation errors being correlated over roughly the size of the DEM pixel, and hence, the effective number of independent looks needs to be reduced by the ratio of the area of the DEM pixel, A_{dem} , to the area of a radar pixel, A_{pix} .

D. Projected Area-Induced Errors

The backscattering coefficient σ_o is defined as the ratio of the radar cross section to the pixel area. Topographic variations, however, cause the pixel area to change, leading to often undesired artifacts in the backscattering coefficient. Topographic effects are thus routinely removed from SAR data using DEMs. However, errors in the DEM can lead to an incorrect area projection normalization of radar backscatter. This section models

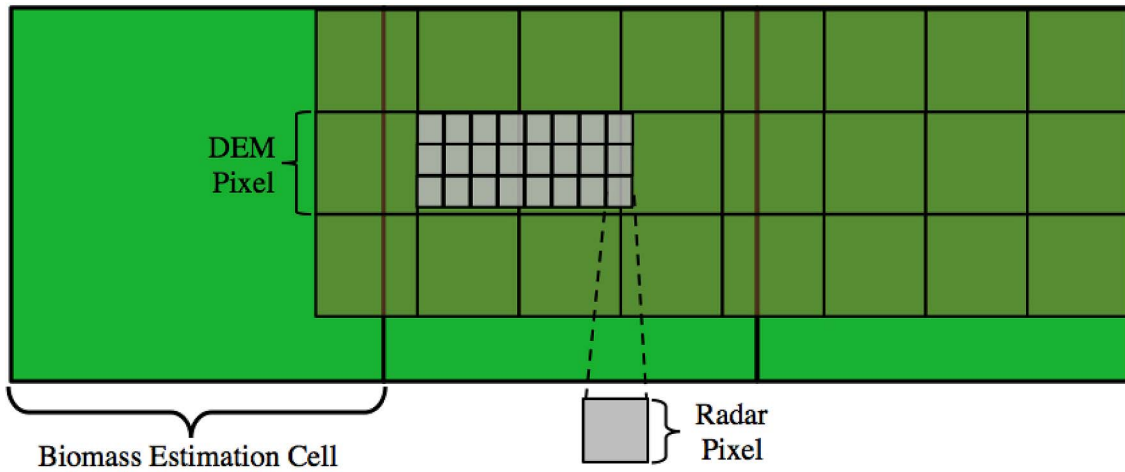


Fig. 7. Figure illustrating the relationship between the biomass estimation cell area, DEM pixel, and radar pixel. Single look radar pixels are generally of the highest resolution (shaded in gray), followed by medium-resolution DEM pixels and, finally, biomass estimation cells, which are assumed to have the lowest resolution (light green) requiring several radar looks to reduce errors.

backscatter errors due to DEM uncertainties. The projected area corrected backscatter σ_{ob} is given by

$$\sigma_{ob} = \mu \frac{A_t}{A_c} = \mu A_t \frac{\langle \hat{n}_\Sigma, \hat{n}_I \rangle}{\Delta s \Delta \rho} \quad (39)$$

where μ is a constant independent of area, A_t is the true ground area of a radar pixel, A_c is the estimated projected area based on geometry, $\Delta \rho$ is the range pixel size, Δs is the azimuth pixel size, \hat{n}_Σ is the outward pointing surface normal to the terrain, and \hat{n}_I is the normal to the radar imaging slant plane, while $\langle \cdot, \cdot \rangle$ is the scalar inner product of two vectors. The surface normal is computed in terms of surface slopes by

$$\begin{aligned} \hat{n}_\Sigma &= \frac{-1}{\sqrt{1 + \left(\frac{\partial \Sigma}{\partial s}\right)^2 + \left(\frac{\partial \Sigma}{\partial c}\right)^2}} \begin{bmatrix} \frac{\partial \Sigma}{\partial s} \\ \frac{\partial \Sigma}{\partial c} \\ -1 \end{bmatrix} \\ &= \frac{-1}{\sqrt{1 + \tan^2(\tau_\rho) + \tan^2(\tau_s)}} \begin{bmatrix} \tan(\tau_s) \\ \tan(\tau_\rho) \\ -1 \end{bmatrix} \end{aligned} \quad (40)$$

where c and s denote the cross-track and along-track directions, respectively, $\partial \Sigma / \partial c$ and $\partial \Sigma / \partial s$ are the cross-track and along-track slopes, respectively, and the cross-track and along-track slope angles are defined by $\tan \tau_\rho = \partial \Sigma / \partial c$ and $\tan \tau_s = \partial \Sigma / \partial s$. The imaging plane normal is defined as $\hat{n}_I = \hat{s} \times \hat{\ell}$, where \hat{s} is a unit vector in the along-track direction and $\hat{\ell}$ is the unit line-of-sight vector. For broadside imaging with incidence angle θ , a typical configuration, we have

$$\hat{\ell} = \begin{bmatrix} 0 \\ \sin(\theta) \\ -\cos(\theta) \end{bmatrix} \quad (41)$$

which yields

$$\hat{n}_I = \hat{s} \times \hat{\ell} = \begin{bmatrix} 0 \\ \cos(\theta) \\ \sin(\theta) \end{bmatrix}. \quad (42)$$

Using (40) and (42) in (39) gives

$$\sigma_{ob} = \mu A_t \frac{\sin(\theta - \tau_\rho) \cos(\tau_s)}{\Delta s \Delta \rho \sqrt{1 - \sin^2(\tau_\rho) \sin^2(\tau_s)}}. \quad (43)$$

Thus, the area compensation factor can be written as

$$A_c = \frac{\Delta s \Delta \rho \sqrt{1 - \sin^2(\tau_\rho) \sin^2(\tau_s)}}{\sin(\theta - \tau_\rho) \cos(\tau_s)} = \Delta s \Delta \rho \frac{\xi}{\chi} \quad (44)$$

where $\xi = \sqrt{1 - \sin^2(\tau_\rho) \sin^2(\tau_s)}$ and $\chi = \sin(\theta - \tau_\rho) \cos(\tau_s)$ are defined for notational convenience. Differentiating (44) yields

$$\begin{aligned} \Delta A_c &= \Delta s \Delta \rho \frac{\chi \dot{\xi} - \xi \dot{\chi}}{\chi^2} \\ &= \frac{\Delta s \Delta \rho \xi}{\chi} \frac{\chi \dot{\xi} - \xi \dot{\chi}}{\xi \chi} \\ &= A_c \left(\frac{\dot{\xi}}{\xi} - \frac{\dot{\chi}}{\chi} \right). \end{aligned} \quad (45)$$

From (45), we get

$$\begin{aligned} \frac{\Delta A_c}{A_c} &= -\frac{1}{2} \frac{\sin(2\tau_\rho) \sin^2(\tau_s) \Delta \tau_\rho + \sin(2\tau_s) \sin^2(\tau_\rho) \Delta \tau_s}{1 - \sin^2(\tau_\rho) \sin^2(\tau_s)} \\ &\quad + \frac{\cos(\theta - \tau_\rho) \cos(\tau_s) \Delta \tau_\rho - \sin(\theta - \tau_\rho) \sin(\tau_s) \Delta \tau_s}{\sin(\theta - \tau_\rho) \cos(\tau_s)} \end{aligned} \quad (46)$$

where $\Delta \tau_\rho$ and $\Delta \tau_s$ are errors in the cross-track and along-track slopes, respectively. If the cross-track and along-track slope errors are the same, then (46) can be slightly simplified to

$$\begin{aligned} \frac{\Delta A_c}{A_c} &= -\frac{1}{2} \frac{\sin(2\tau_\rho) \sin^2(\tau_s) + \sin(2\tau_s) \sin^2(\tau_\rho)}{1 - \sin^2(\tau_\rho) \sin^2(\tau_s)} \Delta \tau \\ &\quad + \frac{\cos(\theta - \tau_\rho - \tau_s)}{\sin(\theta - \tau_\rho) \cos(\tau_s)} \Delta \tau. \end{aligned} \quad (47)$$

To get the slope angle error from the DEM height errors, we first differentiate $\tan \tau_x = \partial \Sigma / \partial x$ to get

$$\sec^2(\tau_x) \Delta \tau_x = \Delta \left(\frac{\partial \Sigma}{\partial x} \right). \quad (48)$$

Substituting $1 + \tan^2(\tau_x) = \sec^2(\tau_x)$ in (48) gives

$$\Delta \tau_x = \frac{\Delta \left(\frac{\partial \Sigma}{\partial x} \right)}{1 + \left(\frac{\partial \Sigma}{\partial x} \right)^2}. \quad (49)$$

Finally, the slope error can be computed in terms of the DEM error $\sigma_{h_{dem}}$ by

$$\Delta \left(\frac{\partial \Sigma}{\partial x} \right) = \frac{\sigma_{h_{DEM}}}{L_{DEM}} \quad (50)$$

where L_{DEM} is the DEM postspacing.

The terms multiplying $\Delta \sigma_a$ in (6) follow from the same reasoning given in the end of Section III-C3.

IV. ESTIMATING BIOMASS UNCERTAINTY

Given that each polarimetric backscatter measurement is noisy and we have a detailed description of the noise sources, we now wish to determine how this translates into biomass estimation error. The formulation presented here aims to be generic since the final algorithm to determine biomass is still in development. To avoid biomass estimation algorithm specifics and yet capture the basic sensitivity of biomass retrieval to instrument and mission parameters, we look at the first-order Taylor's expansion of biomass b as a function of backscatter parameters, $[\sigma_{hh} \ \sigma_{hv} \ \sigma_{vv}]$, and then compensate for having correlated noise between the various components which leads to the basic equation for estimating biomass estimation error, Δb , as

$$\Delta^2 b = \left[\frac{\partial b}{\partial \sigma_{hh}} \Delta \sigma_{hh} \quad \frac{\partial b}{\partial \sigma_{hv}} \Delta \sigma_{hv} \quad \frac{\partial b}{\partial \sigma_{vv}} \Delta \sigma_{vv} \right] \times \tilde{\Gamma} \left[\begin{array}{c} \frac{\partial b}{\partial \sigma_{hh}} \Delta \sigma_{hh} \\ \frac{\partial b}{\partial \sigma_{hv}} \Delta \sigma_{hv} \\ \frac{\partial b}{\partial \sigma_{vv}} \Delta \sigma_{vv} \end{array} \right]^{\frac{1}{2}} \quad (51)$$

where $\tilde{\Gamma} = P_c^t \Gamma P_c$ is the combination of an empirically derived correlation matrix Γ of polarimetric measurements to biomass given by

$$\Gamma = \frac{1}{N_p^2} \begin{bmatrix} \epsilon_{11} & \gamma_{12} & \gamma_{13} \\ \gamma_{21} & \epsilon_{22} & \gamma_{23} \\ \gamma_{31} & \gamma_{32} & \epsilon_{33} \end{bmatrix} \quad (52)$$

where ϵ_{ii} is equal to 0 or 1 depending on whether a given polarization is used, γ_{ij} is the correlation between the i th and j th measurements, N_p is the number of polarimetric channels used, and P_c is a polarimetric calibration error matrix of the form

$$P_c = I + \delta_M = I + \begin{bmatrix} 0 & \delta_{12} & -\delta_{13} \\ -\delta_{21} & 0 & \delta_{23} \\ \delta_{31} & -\delta_{32} & 0 \end{bmatrix}. \quad (53)$$

TABLE IV
MEASURED CORRELATION MATRIX VALUES

Channels	Value
HH and HV (γ_{12})	0.34
HH and VV (γ_{13})	0.18
HV and VV (γ_{23})	0.22

Observe that the second term in (53) is a skew symmetric matrix which is adequate for handling small rotational errors that may be instrument induced or represent uncompensated Faraday rotation caused by the ionosphere.

The correlation matrix Γ is one of the four key empirically derived quantities needed for the error model. In principle, this matrix is biome dependent. The correlation matrix is obtained empirically by taking a set of biomass measurements that consist of M 4-tuples, $\{b_i, \sigma_{hh_i}, \sigma_{hv_i}, \sigma_{vv_i}\}$, $1 \leq i \leq M$, and fitting each polarimetric channel's σ_o values to a function of biomass level. Let $f_{pq}(b)$, ($pq = hh, hv, vv$), denote the fits for the polarimetric channels, and then, form the fit-adjusted data sets, Σ_k , by setting the i th element to be

$$\tilde{\sigma}_{pq_i} = \sigma_{pq_i} - f_{pq}(b_i). \quad (54)$$

The correlation between two polarimetric data channels, γ_{ij} , is then computed as

$$\gamma_{ij} = \frac{|\langle \Sigma_i, \Sigma_j \rangle|}{|\Sigma_i| |\Sigma_j|} \quad (55)$$

where $\langle X, Y \rangle$ denote the M -dimensional Euclidean inner product and $|X|$ denotes the M -dimensional Euclidean norm. Table IV gives the values of the correlation based on a combination of AIRSAR and PALSAR tropical rain forest measurements. That is, the 4-tuples described earlier consisted of both PALSAR and AIRSAR measurements of tropical rainforest with varying biomass levels, and the fits are based on the aggregated data sets. The resulting correlation values shown in Table IV are the result of applying (55) to these data.

V. MINIMAL BIOMASS CELL SIZE FORMULA

In addition to being able to compute the expected biomass error as outlined in Section IV, it is also useful to be able to compute the minimal biomass estimation cell size needed to achieve a desired biomass mapping accuracy κ . Setting the biomass error from (51) to κ times the biomass level b yields

$$\Delta b^2 = \left(\vec{\nabla} b \bullet \Delta \vec{\sigma} \right)^t \Gamma \left(\vec{\nabla} b \bullet \Delta \vec{\sigma} \right) = \kappa^2 b^2 \quad (56)$$

where $X \bullet Y$ denotes the Hadamard or entrywise product of X and Y . The goal of this section is to use (56) to solve for the minimal biomass estimation cell size L . Note that L enters into (56) through the number of spatial looks, N . From (25) and noting that the pixel area $A_{pix} = \kappa_\rho \Delta \rho \kappa_s \Delta s / \sin \theta_i$, it is seen that N is simply related to L by

$$N = \frac{L^2}{A_{pix}}. \quad (57)$$

Expanding (56) using (51) gives

$$\begin{aligned} \Delta b^2 = \frac{1}{N_p^2} & \left[\left(\frac{\partial b}{\partial \sigma_{hh}} \Delta \sigma_{hh} \right)^2 + \left(\frac{\partial b}{\partial \sigma_{hv}} \Delta \sigma_{hv} \right)^2 \right. \\ & + \left(\frac{\partial b}{\partial \sigma_{vv}} \Delta \sigma_{vv} \right)^2 + 2\gamma_{12} \frac{\partial b}{\partial \sigma_{hh}} \frac{\partial b}{\partial \sigma_{hv}} \Delta \sigma_{hh} \Delta \sigma_{hv} \\ & + 2\gamma_{13} \frac{\partial b}{\partial \sigma_{hh}} \frac{\partial b}{\partial \sigma_{vv}} \Delta \sigma_{hh} \Delta \sigma_{vv} \\ & \left. + 2\gamma_{23} \frac{\partial b}{\partial \sigma_{hv}} \frac{\partial b}{\partial \sigma_{vv}} \Delta \sigma_{hv} \Delta \sigma_{vv} \right]. \end{aligned} \quad (58)$$

To solve for L , the terms in the $\Delta \sigma_{pq}$'s in (58) that involve the number of spatial looks, N , are grouped separately from those independent of N . Therefore, define β_{pq} to be the terms independent of N and μ_{pq} to be the terms depending on N that are given by

$$\begin{aligned} \mu_{pq} = & \left[\frac{1}{\sqrt{N_{os}}} + \frac{1}{\sqrt{N_{ot}}} \frac{1 + \frac{\text{SNR}}{\text{MNR}}}{\text{SNR}} \right. \\ & \left. + \frac{1}{\sqrt{N_{ot}}} \sqrt{\frac{A_{dem}}{A_{pix}}} \left(\frac{\Delta G_{geo}}{G} + \frac{\Delta A}{A} \right) \right] \sigma_{pq} \end{aligned} \quad (59)$$

$$\beta_{pq} = \frac{1}{\sqrt{N_{ot}}} \left(\frac{\Delta G_{pnt}}{G} + \left(10^{\frac{\Delta \sigma_{3dB}}{10}} - 1 \right) + \frac{\Delta \sigma_{pq_t}}{\sigma_{pq}} \right) \sigma_{pq} \quad (60)$$

such that

$$\Delta \sigma_{pq} = \frac{\sqrt{A_{pix}}}{L} \mu_{pq} + \beta_{pq}. \quad (61)$$

Substituting (61) into (58), expanding terms and some tedious algebra to group terms in powers of L , and substituting that expression into (56) result in the following quadratic equation for L :

$$\begin{aligned} N_p^2 L^2 \kappa^2 b^2 & = L^2 \left[\left(\frac{\partial b}{\partial \sigma_{hh}} \beta_{hh} \right)^2 + \left(\frac{\partial b}{\partial \sigma_{hv}} \beta_{hv} \right)^2 + \left(\frac{\partial b}{\partial \sigma_{vv}} \beta_{vv} \right)^2 \right. \\ & + 2\gamma_{12} \frac{\partial b}{\partial \sigma_{hh}} \frac{\partial b}{\partial \sigma_{hv}} \beta_{hh} \beta_{hv} + 2\gamma_{13} \frac{\partial b}{\partial \sigma_{hh}} \frac{\partial b}{\partial \sigma_{vv}} \beta_{hh} \beta_{vv} \\ & \left. + 2\gamma_{23} \frac{\partial b}{\partial \sigma_{hv}} \frac{\partial b}{\partial \sigma_{vv}} \beta_{hv} \beta_{vv} \right] \\ & + 2L \sqrt{A_{pix}} \left[\left(\frac{\partial b}{\partial \sigma_{hh}} \right)^2 \mu_{hh} \beta_{hh} + \left(\frac{\partial b}{\partial \sigma_{hv}} \right)^2 \mu_{hv} \beta_{hv} \right. \\ & + \left(\frac{\partial b}{\partial \sigma_{vv}} \right)^2 \mu_{vv} \beta_{vv} + \gamma_{12} \frac{\partial b}{\partial \sigma_{hh}} \frac{\partial b}{\partial \sigma_{hv}} \\ & \times (\mu_{hv} \beta_{hh} + \mu_{hh} \beta_{hv}) + \gamma_{13} \frac{\partial b}{\partial \sigma_{hh}} \frac{\partial b}{\partial \sigma_{vv}} \\ & \times (\mu_{hh} \beta_{vv} + \mu_{vv} \beta_{hh}) + \gamma_{23} \frac{\partial b}{\partial \sigma_{hv}} \frac{\partial b}{\partial \sigma_{vv}} \\ & \left. \times (\mu_{hv} \beta_{vv} + \mu_{vv} \beta_{hv}) \right] \end{aligned}$$

$$\begin{aligned} & + A_{pix} \left[\left(\frac{\partial b}{\partial \sigma_{hh}} \mu_{hh} \right)^2 + \left(\frac{\partial b}{\partial \sigma_{hv}} \mu_{hv} \right)^2 + \left(\frac{\partial b}{\partial \sigma_{vv}} \mu_{vv} \right)^2 \right. \\ & + 2\gamma_{12} \frac{\partial b}{\partial \sigma_{hh}} \frac{\partial b}{\partial \sigma_{hv}} \mu_{hh} \mu_{hv} + 2\gamma_{13} \frac{\partial b}{\partial \sigma_{hh}} \frac{\partial b}{\partial \sigma_{vv}} \\ & \left. \times \mu_{hh} \mu_{vv} + 2\gamma_{23} \frac{\partial b}{\partial \sigma_{hv}} \frac{\partial b}{\partial \sigma_{vv}} \mu_{hv} \mu_{vv} \right]. \end{aligned} \quad (62)$$

Using the traditional notation of A for the coefficient of the L^2 term, B for the linear term, and C for the constant term on the right side of (62) gives the quadratic equation

$$N_p^2 L^2 \kappa^2 b^2 = AL^2 + BL + C \quad (63)$$

which, after applying the quadratic formula, is readily solved for L yielding

$$L = \frac{-B - \sqrt{B^2 - 4(A - N_p^2 \kappa^2 b^2)C}}{2(A - N_p^2 \kappa^2 b^2)}. \quad (64)$$

The formulation in (64) is general and includes all error sources. One special case is of interest, i.e., if only one polarization channel is used and only speckle noise is considered (which is the dominant noise source) then (64) reduces to

$$L \geq \frac{\sigma \sqrt{\kappa_\rho \kappa_s} \Delta \rho \Delta s}{\kappa b \sqrt{\sin \theta_i}} \frac{\partial b}{\partial \sigma}. \quad (65)$$

Note that the minimum size biomass estimation cell size is proportional to the derivative of biomass with respect to σ . Since the derivative of biomass with respect to σ grows very quickly as the biomass level approaches the saturation level (see Section II), the required biomass cell size does as well. Thus, the functions used to fit the data play an integral role in assessing the biomass estimation accuracy and the amount of spatial averaging required to achieve that accuracy. Note that care must be taken when making fits to backscatter as a function of biomass to ensure good behavior of the derivatives, particularly in the region around saturation. Small perturbations in the fit can result in the derivatives changing substantially, factors of 2–5, and hence result in very different biomass estimation accuracy assessments in this region or in very different minimal cell sizes. Also note that this formula implicitly assumes the spatial homogeneity of the vegetation, i.e., that the biomass estimation cell only includes vegetation and not other scatterers such as buildings or water. Thus, the value of the minimum cell size must be smaller than the scales at which spatial averaging would start to include nonvegetated areas as well (see Section III-A2). An example of the minimal cell size computation for a representative system is provided in Section VIII.

VI. FUNCTIONAL DEFINITION OF SATURATION

In this section, we propose a functional definition of saturation that is linked to the maximal biomass level such that a prescribed biomass estimation accuracy can be achieved. Many biomass model functions show increasing backscatter as function of increasing biomass for arbitrary large values

TABLE V
BIOMASS MODEL FIT PARAMETERS

Biome Type	A	B	C	α
Open Woodland and Shrub	0.0864	0.0297	0.0095	0.2558
Woodland and Shrub	0.1303	0.0351	-0.0007	1.2371
Forest	0.1484	0.0339	0.0498	0.1825
Combined	0.1073	0.0305	0.0103	0.2893

of biomass. Not only is this not physical, it certainly is not indicative of the region of biomass levels for which acceptable biomass estimation accuracy can be achieved. The saturation level is defined as the biomass level for which the biomass estimation error due to speckle equals the desired biomass estimation accuracy. Mathematically, this can be represented by

$$\Delta b = \frac{\partial b}{\partial \sigma} \Delta \sigma = \kappa b \quad (66)$$

where Δb is the biomass estimation error, $\Delta \sigma$ is the error in backscatter due to speckle, and κ is the desired biomass estimation accuracy (i.e., $\Delta b/b = \kappa$ represents the fractional estimation error). Note that the error in backscatter due to speckle is given by σ/\sqrt{N} , where N is the number of looks. Therefore, given a mathematical form for σ as a function of biomass, the saturation level is defined as the zero of the function, F , given by

$$F(b) = \frac{\sigma(b)}{\sqrt{N}} - \kappa b \frac{\partial \sigma}{\partial b}(b). \quad (67)$$

It is important to note that the saturation level defined in this manner may not have a solution. To achieve a desired biomass estimation error level, it is necessary that the intrinsic backscatter variation due to speckle results in estimation errors less than the specified accuracy level. Thus, if an insufficient number of looks are used, resulting in too large a backscatter variation relative to the backscatter sensitivity to biomass, then no solution to (67) may exist. This makes physical sense since, in the limit as the desired biomass estimation error goes to zero, there clearly is no solution.

Using the model function described previously by (1), we fit biomass measurements of L-band advanced land observation satellite (ALOS) phased array L-band synthetic aperture radar (PALSAR) data collected in Australia described in [7] for four segmentations of the data consisting of open woodland and shrub, woodland and shrub, forest, and all measurements combined. Results of the fits are given in Table V, and Fig. 8 shows the fits for two of the segmentation classes along with the associated raw measurement data. Based on these model functions, we used (67) to estimate the saturation level for 500 and 1000 looks for desired estimation accuracy, κ , levels of 30%, 50%, and 100% which are shown in Table VI. Observe that the biomass saturation level decreases as the desired biomass estimation accuracy decreases and increases as the number of looks increases as would be expected.

VII. DATA-DRIVEN MODEL COMPONENTS

In this section, we summarize the data-driven portions of the model that require some additional effort and outline some aspects of the error modeling that have not been considered thus far but are needed for a complete error model.

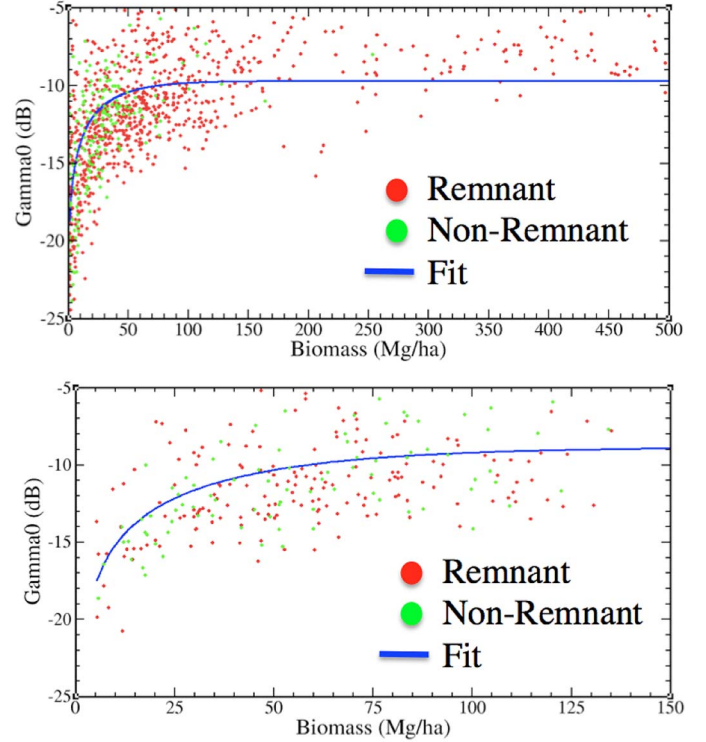


Fig. 8. Plots of the backscatter as function of biomass measurements and their associated model function using the fit coefficients in Table V for the (top) combined data and (bottom) woodland and shrubs. Visual inspection of these plots would lead to estimated saturation levels between 75 and 125 Mg/ha. Saturation values based on the functional definition described here give values between 98 and 139 Mg/ha for 1000 looks and 30% desired estimation accuracy.

TABLE VI
SATURATION LEVEL SUMMARY

Type	Saturation Level (Mg/ha)					
	500 Looks			1000 Looks		
	30%	50%	100%	30%	50%	100%
Combined	83	105	133	98	119	147
Open Woodland, Shrub	85	108	137	100	123	151
Woodland, Shrub	122	146	176	139	162	191
Forest	44	63	87	57	76	99

There are four data-driven elements to the error model that were discussed previously that are summarized here along with a summary of future work needed for these elements. The four items are as follows.

- 1) Correlation matrices that quantify the similarity between the three polarimetric backscatter channels for various biomass levels. These matrices are biome, cell size, and incidence angle dependent. Currently, the correlation data have been computed for one cell size and biome. Work is in progress to extend this to a number of biomes for a range of cell sizes and incidence angles.
- 2) Curves relating the mean backscatter levels to biomass. The curves used in this paper are based on distorted Born approximation, and this model or some minor variant of it is expected to suffice for future analysis, although some additional study of this point is being done. These curves need to be developed for a set of biomes that are

representative of the world's forest structural varieties, and work on several of these is in progress.

- 3) Various noise sources to the backscatter measurement are reduced by spatial averaging. Implicit in this spatial averaging is the assumption of homogeneity over the cell being averaged. At some point, the natural heterogeneity of the vegetation results in an increase rather than a reduction in the backscatter noise. This maximal size needs to be determined empirically for the various biomes.
- 4) The measured backscatter varies from observation to observation due to wind, weather, flooding, or other minor disturbances that are not the result of changes in above ground biomass. The amount of temporal variability is expected to depend on biomass estimation cell size, the maximal time interval between observations, biomass level, and biome type. A model based on empirical data is being developed for several biomes.

VIII. PERFORMANCE ASSESSMENT EXAMPLE

The basic model for biomass error estimation from radar polarimetric backscatter data, presented in Section IV, is illustrated using parameters similar to a NASA proposed Earth observing L-band radar instrument, called deformation, ecosystem science, and dynamics of ice (DESDynI) [12]. The input parameters and error model results are described hereinafter. A further discussion and application of this error model using backscatter data from NASA/Jet Propulsion Laboratory (JPL)'s airborne L-band Uninhabited aerial vehicle synthetic aperture radar (UAVSAR) instrument and field biomass estimates is presented in [15].

A. Input Parameters

This section explains the independent parameters of the error model. These are divided into six major groups, constants, empirically derived data-driven parameters, inputs for external data, radar instrument parameters, and science product parameters. Table VII shows the complete set of input parameters to the model for this particular example.

1) *Empirical Data-Derived Parameters*: Parameters in this section fall into three categories consisting of the backscatter to biomass function parameters, the temporal variability model parameters, and, finally, the entries of the correlation matrix Γ .

- 1) *Model coefficients*—The biomass to backscatter model function has four parameters as described in Section II.
- 2) *Temporal variability*—Temporal variation for each polarization is modeled as a linear function of time. These coefficients listed here are based on the discussion in Section III-B and Table III.
- 3) *Correlation matrix*—These three numbers (between 0 and 1) correspond to the cross-correlations between the three polarimetric channels as described in Section IV and Table IV.
- 2) *External Data Input Parameters*: Parameters in this section refer to the DEM parameters and mean slopes.
 - 1) *DEM posting*—Distance between elevation measurements in the data set. Here, we use a 90-m posting

TABLE VII
INPUT PARAMETERS FOR BIOMASS ERROR MODEL

Parameter	Value	Comments
Empirical Data Derived Parameters		
<i>Sensitivity Function</i> $\sigma_{pq}(b) = A_{pq}(1 - e^{(-B_{pq}b)}) + C_{pq}b^{\alpha_{pq}}e^{(-B_{pq}b)}$		
A_{hh}	0.25	HH
B_{hh}	0.007	
C_{hh}	0.0700	
α_{hh}	0.2	
A_{hv}	0.068	HV
B_{hv}	0.006	
C_{hv}	0.0180	
α_{hv}	0.2	
A_{vv}	0.19	VV
B_{vv}	0.005	
C_{vv}	0.040	
α_{vv}	0.2	
Temporal Variability Functions		
HH Constant (dB)	0.5	HH
HH Linear Term	0	
HV Constant	0.5	HV
HV Linear Term	0	
VV Constant	0.5	VV
VV Linear Term	0	
Correlation Matrix		
HH-HH	1	
HH-HV	0.34	
HH-VV	0.18	
VV-HV	0.22	
VV-VV	1	

consistent with the released DEM posting of the shuttle radar topography mission (SRTM) data.

- 2) *DEM accuracy*—Accuracy of elevation measurements in the DEM. For the DEM accuracy, we used the multi-looked elevation error average for SRTM DEM.
- 3) *Slope data*—Mean cross-track and along-track slope in the region of interest. The values used here represent fairly extremely local slopes from a world average perspective in order to illustrate the impact of these terms.
- 3) *Radar Instrument Parameters*: These parameters describe the properties of radar instrument and processing relevant for biomass error estimation.
 - 1) *Range bandwidth*—This parameter is used to compute the range resolution. We used a 40-MHz bandwidth consistent with a DESDynI radar mode proposed for biomass estimation.
 - 2) *Antenna azimuth dimension*—This is used to determine the nominal azimuth resolution prior to weighting for sidelobe reduction and is equal to the antenna dimension divided by two. We are assuming a DESDynI-like reflector antenna with a diameter of 15 m.
 - 3) *Beamwidths*—The 3-dB beamwidths of the transmit and receive beams in both elevation and azimuth are based on a DESDynI-like 15-m reflector antenna.
 - 4) *Null-to-3-dB relationships*—Depending on the antenna weighting function, the gain may drop off more or less quickly than the assumed sinc pattern described earlier. To roughly simulate different antenna weighting function effects on the main lobe, we use a simple null-to-3-dB

TABLE VII
INPUT PARAMETERS FOR BIOMASS ERROR MODEL (Continued...)

Parameter	Value	Comments
HV-HV	1	
External Data Input Parameters		
DEM Post Spacing (m)	90	Assumes we will use either the 30/90 m SRTM DEM.
DEM Elevation Accuracy (m)	3	
Mean Cross Track Slope ($^{\circ}$)	5	These are mean values of the
Mean Along Track Slope ($^{\circ}$)	10	slopes in the region where the evaluation is being made.
Radar Instrument Parameters		
Radar Wavelength (m)	0.24	L-band center frequency
Range Bandwidth (MHz)	40	Radar system bandwidth
Azimuth Antenna Size (m)	15	Azimuth antenna size (L) determines azimuth resolution (typically $L/2$)
Transmit Beamwidth Elevation Direction ($^{\circ}$)	16	3 dB beamwidth
Receive Beamwidth Elevation Direction ($^{\circ}$)	1	3 dB beamwidth
Transmit Beamwidth Azimuth Direction ($^{\circ}$)	1	3 dB beamwidth
Receive Beamwidth Azimuth Direction ($^{\circ}$)	1	3 dB beamwidth
Null to 3 dB Antenna Beamwidth Ratio on Transmit	1.136	Ratio of null to 3 dB width - needed for Sinc
Null to 3 dB Antenna Beamwidth Ratio on Receive	1.136	Ratio of null to 3 dB width - needed for Sinc
Total Ambiguities (dB)	20	
Number of Bits in ADC	4	Quantization level
Range Impulse Weighting Factor	0.7	1=uniform, .08= Hamming, 0=Hanning
Azimuth Impulse Weighting Factor	0.7	1=uniform, .08= Hamming, 0=Hanning
Co-pol Noise Equivalent σ_o (dB)	-25	equivalent noise power, NOTE is bandwidth dependent
X-pol Noise Equivalent σ_o (dB)	-25	equivalent noise power, NOTE is bandwidth dependent
Polarimetric Calibration Delta HH-HV	0	Used to account for imperfect polarization state measurements
Polarimetric Calibration Delta HH-VV	0	Assumed perfectly calibrated for this example
Polarimetric Calibration Delta HV-VV	0	Assumed perfectly calibrated for this example
Residual Random Calibration Error (dB)	0.05	Random uncompensated residual error
Mission Parameters		
Platform Altitude (km)	761	Altitude for an 8 day repeat
Number of Speckle Diverse Observations	1	Must be ≥ 1 - needs look angle diversity
Number of Speckle Identical Observations	3	Number repeat passes with correlated speckle
Pointing Knowledge Error (arc-sec)	50	Pointing Knowledge after orbit reconstruction

ratio parameter. For a nominal sinc pattern, this value is 1/0.88. Two values are specified, one for transmit and the other for receive.

TABLE VII
INPUT PARAMETERS FOR BIOMASS ERROR MODEL (Continued...)

Parameter	Value	Comments
Science Product Parameters		
Biomass Estimation Cell Size (m)	250	Linear dimension
1 σ Scaling Factor	1	Used to set confidence interval (see below) 1.66=90%
Biomass Level (Mg/ha)	90	Biomass level to determine error for
Desired Relative Biomass Estimation Accuracy	20%	Used to determine the minimal estimation cell size

- 5) *Total ambiguities*—These are computed based on radar system parameters and an assumed backscatter function as described in references such as [14]. Here, we used estimates from a DESDynI-like radar performance model.
- 6) *Range/azimuth weighting factor*—This parameter corresponds to the η weighting parameter described in (14), where $\eta = 1$ corresponds to having no weighting and $\eta = 0$ corresponds to Hanning weighting which results in the smallest sidelobes and, hence, the best ISLR at the expense of maximal main-lobe broadening. Here, we selected a value of 0.7, which results in slight sidelobe and very little main-lobe broadening to maximize the number of looks.
- 7) *Number of bits in ADC*—This is the number of effective bits after whatever block adaptive quantization (BAQ) compression is done—not the raw number of hardware bits in the ADC. Here, we selected 4 b consistent with the proposed DESDynI radar instrument.
- 8) *Noise equivalent σ_o* —This is the value of the backscatter that will result in 0-dB SNR. Values for the co-polarized and cross-polarized channels are specified separately. These values are similar to a number of spaceborne instruments.
- 9) *Random calibration error*—Here, 0 dB corresponds to no errors. See Section III-C1 for a more complete description.
- 4) *Mission Parameters*: These parameters describe the observing scenario for the radar observations.
 - 1) *Platform altitude*—This is the height of the radar instrument, with a chosen value of 761 km corresponding to an assumed eight-day exact repeat orbit.
 - 2) *Speckle diverse observations*—This is the number of observations with sufficiently different viewing geometry such that speckle is not correlated, e.g., ascending and descending passes. The number of speckle diverse observations of one assumes that speckle diverse observation arises from at least one observation on an ascending and descending orbit.
 - 3) *Speckle identical observations*—This is the number of observations that are collected from basically the same imaging geometry for which speckle is correlated. Note that the total number of observations equals the number of speckle diverse observations plus the number of speckle identical observations minus one. We assumed

three speckle identical observations corresponding to the number of observations available using a 90-day, e.g., one season, viewing period.

- 4) *Pointing knowledge error*—This refers to the uncertainty in the knowledge of where the antenna was pointing relative to the Earth. Pointing knowledge is based on the pointing accuracy achievable, including star tracker and inertial measurement unit (IMU) measurements errors coupled with mechanical and thermal distortions for a proposed DESDynI-like radar system.

5) *Science Product Parameters*: This section sets the biomass estimation cell size, biomass level, desired estimation accuracy, and what polarimetric channels to use.

- 1) *Biomass estimation cell size*—This is the biomass estimation cell size (assumed square) which is typically between 100 m and 1 km.
- 2) *Biomass level*—The value of forest biomass for which the biomass estimation accuracy is desired. This is based on the assumption of saturation of L-band data at 90 Mg/ha.
- 3) *Desired relative biomass estimation accuracy*—This is the relative biomass estimation accuracy $\Delta b/b$ denoted by κ in (67). A DESDynI-like requirement of 20% error is chosen here.

B. Output Parameters

This section describes the quantities computed using the error model, including the biomass estimation accuracy for the example biomass level. Accuracy values are computed at multiple incidence angles within a swath since the accuracy depends on where in the radar swath a cell is located. Both swath-averaged and maximal error values are reported for values in the 30° to 40° portion of the swath. Table VIII shows the quantities computed using the model. Additional detail concerning some of the parameters is given in the following sections.

1) *Mission Parameters*: Only one parameter is computed in this section.

- 1) *Total number of observations*—This quantity is computed from the speckle diverse and speckle identical observations as described in Section VIII-A.

2) *Radar Instrument Parameters*: The radar parameters are related to the resolution and MNR and SNR terms.

- 1) *Raw range and azimuth resolutions*—These are the range and azimuth resolutions before impulse response weighting is applied.
- 2) *Range and azimuth resolutions*—These are the range and azimuth resolutions after impulse response weighting is applied.
- 3) *QNR, ISLR*—These quantities are computed based on the number of bits in the ADC and the impulse response weighting parameters in range and azimuth. Both linear and decibel units are reported.
- 4) *MNR*—This quantity is computed from the QNR, ISLR, and total ambiguities and is reported in linear and decibel units.
- 5) *SNR*—These quantities are computed for each polarization based on backscatter levels computed from the

TABLE VIII
OUTPUT PARAMETERS FOR BIOMASS ERROR MODEL

Parameter	Value	Comments
Mission Parameters		
Total Number of Observations	3	Combined Speckle and Speckle diverse observations
Radar Instrument Parameters		
Raw Range Resolution	3.75	Range resolution determined from bandwidth
Range Resolution With Weighting	4.11	Range resolution after range weighting
Raw Azimuth Resolution	7.5	Azimuth resolution depending on antenna size
Azimuth Resolution With Weighting	8.23	Azimuth resolution after weighting
QNR (dB)	14	Quantization to noise ratio - depends on bits in ADC
Range ISLR (dB)	-14.5	Integrated Sidelobe ratio - depends on weighting
Azimuth ISLR (dB)	-14.5	Integrated Sidelobe ratio - depends on weighting
Total MNR (dB)	9.16	Total MNR in dB
SNR HH (dB)	18.19	SNR for the HH channel
SNR HV (dB)	12.34	SNR for the HV channel
SNR VV (dB)	16.11	SNR for the VV channel
External Parameters		
Slope Angle Accuracy	0.0333	Slope angle $\tan(\tau_x) = \partial h / \partial x$ error in radians
Science Product Parameters		
Number of Polarimetric Channels Combined	3	Number of Channels being Combined
Confidence Interval (%)	68	Errors reported with respect to this confidence interval
HH Backscatter Level	-6.81	HH Backscatter in dB for the specified biomass
HV Backscatter Level	-12.66	HV Backscatter in dB for the specified biomass
VV Backscatter Level	-8.81	VV Backscatter in dB for the specified biomass
$\partial \sigma_{hh} / \partial b$	4.939×10^{-4}	Derivative of model σ_{hh} function wrt b
$\partial \sigma_{hv} / \partial b$	1.403×10^{-4}	Derivative of model σ_{hv} function wrt b
$\partial \sigma_{vv} / \partial b$	4.315×10^{-4}	Derivative of model σ_{vv} function wrt b
$\partial b / \partial \sigma_{hh}$	2024.5	Derivative of b wrt σ_{hh}

biomass level and the noise equivalent σ_o . Both linear and decibel units are reported.

- 3) *External Parameters*: Only one parameter is computed.

1) *Slope accuracy*—This quantity is computed based on the DEM posting and height accuracy.

4) *Science Product Parameters*: Several quantities related to the biomass sensitivities are computed in this section.

- 1) *Number of channels*—This quantity is based on the selected polarizations to use.
- 2) *Backscatter levels*—These quantities are computed based on the supplied model function and biomass level and are reported in linear and decibel units.
- 3) *Derivatives*—The sensitivities of backscatter to biomass and biomass to backscatter levels are reported for each of the polarization channels.

TABLE VIII
OUTPUT PARAMETERS FOR BIOMASS ERROR MODEL (Continued...)

Parameter	Value	Comments
$\partial b / \partial \sigma_{hv}$	7127.7	Derivative of b wrt σ_{hv}
$\partial b / \partial \sigma_{vv}$	2317.5	Derivative of b wrt σ_{vv}
Minimum Cell Size	Value	Comments
Minimal Biomass Estimation Cell Size	332	Done for 30° incidence angle
Minimal Biomass Estimation Cell Size	297	Done for 35° incidence angle
Minimal Biomass Estimation Cell Size	269	Done for 40° incidence angle
Swath Averaged Biomass Error	Value (%)	Comments
HH Biomass Percentage Error	36.71	Averaged over incidence angle range from 30° to 40°
HV Biomass Percentage Error	33.90	Averaged over incidence angle range from 30° to 40°
VV Biomass Percentage Error	26.57	Averaged over incidence angle range from 30° to 40°
Combined Biomass Percentage Error	23.09	Averaged over incidence angle range from 30° to 40°
Maximum Biomass Error in Swath	Value (%)	Comments
HH Biomass Percentage Error	40.23	Maximum over incidence angle range from 30° to 40°
HV Biomass Percentage Error	37.14	Maximum over incidence angle range from 30° to 40°
VV Biomass Percentage Error	29.11	Maximum over incidence angle range from 30° to 40°
Combined Biomass Percentage Error	25.29	Maximum over incidence angle range from 30° to 40°

5) *Tabulated Results*: Three types of quantities related to biomass estimation performance are reported in this area.

- 1) *Minimum cell size*—From the desired biomass estimation accuracy and biomass level, the minimum cell size needed to achieve this accuracy is computed for incidence angles of 30°, 35°, and 40°.
- 2) *Swath-averaged biomass error*—For each polarization and for the combined estimate, the swath-averaged (between 30° and 40° incidence angles) biomass estimation accuracies are reported.
- 3) *Maximum biomass error in swath*—For each polarization and for the combined estimate (between 30° and 40° incidence angles), the maximal biomass estimation accuracies are reported.

C. Discussion

Using the backscatter to biomass model function described in Section II and with model values from Tables I ($\alpha = 1.0$ case) and II ($\alpha = 0.2$ case), the backscatter error as a function of biomass level between 5 and 100 Mg/ha in 5 Mg/ha increments was computed for five biomass estimation cell sizes of 100, 250, 300, 400, and 500 m. The results are shown in Figs. 9 and 10. Note how a small relatively slight difference to model functions changes the expected errors very dramatically. This illustrates the need to make sure that the appropriate model function is used in determining the biomass estimation accuracy. Differences in the behavior of the derivatives of the model as a function of biomass level result in increased sensitivity for

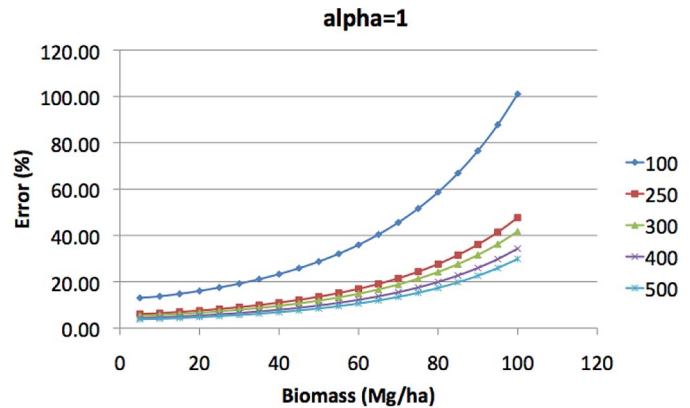


Fig. 9. Biomass estimation accuracy as a function of biomass level for five different cell sizes (100, 250, 300, 400, and 500 m) using the $\alpha = 1$ backscatter model function.

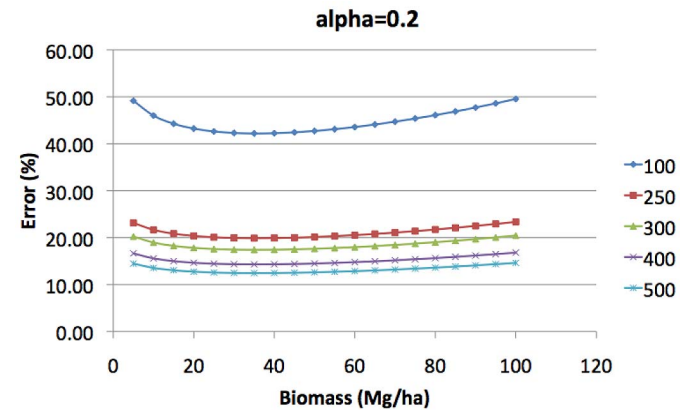


Fig. 10. Biomass estimation accuracy as a function of biomass level for five different cell sizes (100, 250, 300, 400, and 500 m) using the $\alpha = 0.2$ backscatter model function.

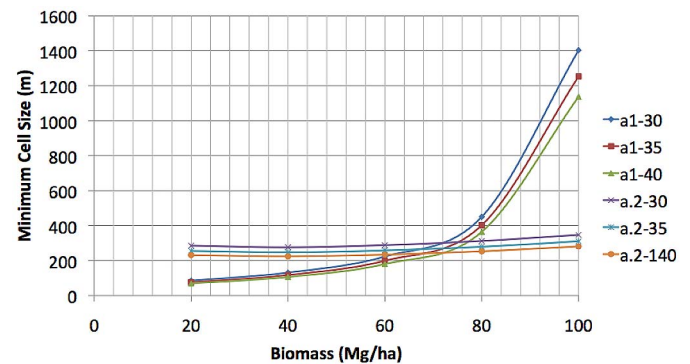


Fig. 11. Plot of the minimum cell size for biomass levels between 20 and 100 Mg/ha for three incidence angles in the swath.

low biomass levels for the $\alpha = 1.0$ model function compared to the $\alpha = 0.2$ model function, whereas for large biomass levels, the opposite is true. This results in better biomass estimation accuracy for low biomass levels and larger biomass estimation accuracy at large biomass levels for the $\alpha = 1.0$ model function.

Fig. 11 shows how the minimal cell size changes as a function of incidence angle and biomass level for the two different backscatter models. Observe that, for $\alpha = 1.0$, the minimum

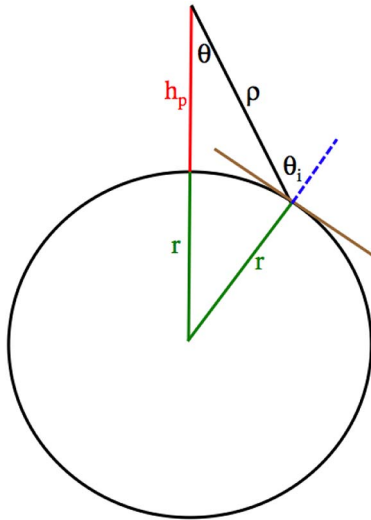


Fig. 12. Figure illustrating the range, look, and incidence angles.

cell size grows extremely fast for biomass levels greater than 80 Mg/ha. This is a result of the rapid growth of the derivative of biomass with respect to backscatter in this region as was shown earlier in Section II. However, for $\alpha = 0.2$ model parameters, the cell size stays relatively flat over this range of biomass levels.

IX. CONCLUSION

In this paper, a mathematical framework for assessing the accuracy of biomass estimates from polarimetric radar was described. The general framework, with careful mathematical formulation, is capable of accounting for all known contributors to the radar backscatter error budget. Furthermore, a framework for translating the parametric backscatter measurement error to an error in biomass estimates was also established. Additionally, a method for translating required biomass accuracies into radar design parameters was also outlined.

APPENDIX

In this section, formulas for various geometric quantities required for the model but not covered previously in this paper are provided. The range ρ to point having look angle θ from a platform at height h_p can be determined using the law of cosines to be

$$\rho = (h_p + r) \cos \theta - \sqrt{r^2 - (h_p + r)^2 \sin^2 \theta} \quad (68)$$

where r is the radius of the Earth as shown in Fig. 12. The incidence angle θ_i , the angle between the line-of-sight vector and the local surface normal, can be obtained using Fig. 12 and the law of sines to give

$$\theta_i = \sin^{-1} \left(\frac{r + h_p}{r} \sin \theta \right). \quad (69)$$

ACKNOWLEDGMENT

The authors would like to thank P. Rosen and the DESDynI project for providing support and encouragement for this work, R. Dubayah and P. Siqueira for many useful and illuminating discussions on the estimation of biomass measurement errors, and R. Lucas for the biomass data used for the examples in Section VI.

REFERENCES

- [1] R. A. Anthes, *Earth Science and Applications from Space: National Imperatives for the Next Decade and Beyond*, National Research Council Committee on Earth Science and Applications from Space. Washington, DC, USA: National Academic Press, 2007.
- [2] F. G. Hall, K. Bergen, J. B. Blair, R. Dubayah, R. Houghton, G. Hurtt, J. Kellendorfer, M. Lefsky, J. Ranson, S. Saatchi, H. H. Shugart, and D. Wickland, "Characterizing 3D vegetation structure from space: Mission requirements," *Remote Sens. Environ.*, vol. 115, no. 11, pp. 2753–2775, Nov. 2011.
- [3] G. Krieger, I. Hajnsek, K. P. Papathanassiou, M. Eineder, M. Younis, F. De Zan, P. Prats, S. Huber, M. Werner, H. Fiedler, A. Freeman, P. Rosen, S. Hensley, W. Johnson, L. Villeux, B. Grafmueller, R. Werninghaus, R. Bamler, and A. Moreira, "The Tandem-L mission proposal: Monitoring Earth's dynamics with high resolution SAR interferometry," in *Proc. IEEE Radar Conf.*, May 2009, pp. 1–6.
- [4] M. L. Imhoff, "Radar backscatter and biomass saturation: Ramifications for global biomass inventory," *IEEE Trans. Geosci. Remote Sens.*, vol. 33, no. 2, pp. 511–518, Mar. 1995.
- [5] D. Leckie and J. Ranson, "Forestry applications applications using imaging radar," in *Principles and Applications of Imaging Radar: Manual of Remote Sensing.*, 3rd ed. Hoboken, NJ, USA: Wiley, 1998, ch. 9, pp. 435–501.
- [6] S. Saatchi, K. Halligan, D. Despain, and R. Crabtree, "Estimation of forest fuel load from radar remote sensing," *IEEE Trans. Geosci. Remote Sens.*, vol. 45, no. 6, pp. 1726–1740, Jun. 2007.
- [7] R. Lucas, J. Armston, R. Fairfax, R. Fensham, A. Accad, J. Carreiras, J. Kelley, P. Bunting, D. Clewley, S. Bray, D. Metcalfe, J. Dwyer, M. Bowen, T. Eyre, M. Laidlaw, and M. Shimada, "An evaluation of the ALOS PALSAR L-band backscatter—Above ground biomass relationship Queensland, Australia: Impacts of surface moisture condition and vegetation structure," *IEEE J. Sel. Topics Appl. Earth Observ. Remote Sens.*, vol. 3, no. 4, pp. 576–593, Dec. 2010.
- [8] S. T. Wu, "Potential application of multi-polarization SAR for plantation pine biomass estimation," *IEEE Trans. Geosci. Remote Sens.*, vol. GRS-25, no. 3, pp. 403–409, May 1987.
- [9] T. Le Toan, A. Beaudoin, J. Riou, and D. Guyon, "Relating forest biomass to SAR data," *IEEE Trans. Geosci. Remote Sens.*, vol. 30, no. 2, pp. 403–411, Mar. 1992.
- [10] M. C. Dobson, F. T. Ulaby, L. E. P. and, T. L. Sharik, K. M. Bergen, J. Kellendorfer, J. R. Kendra, E. Li, Y. C. Lin, A. Nashashibi, K. Sarabandi, and P. Siqueira, "Estimation of forest biophysical characteristics in northern Michigan with SIR-C/X-SAR," *IEEE Trans. Geosci. Remote Sens.*, vol. 33, no. 4, pp. 877–895, Jul. 1995.
- [11] K. Scipal, M. Arcioni, J. Chave, J. Dall, F. Fois, T. LeToan, C. Lin, K. Papathanassiou, S. Quegan, F. Rocca, S. Saatchi, H. Shugart, L. Ulander, and M. Williams, "The BIOMASS mission—An ESA Earth Explorer candidate to measure the BIOMASS of the Earth's forests," in *Proc. IEEE IGARSS*, Jul. 2010, pp. 52–55.
- [12] A. Freeman, P. Rosen, R. Jordan, W. Johnson, S. Hensley, T. Sweetser, A. Loverro, J. Smith, G. Sprague, and Y. Shen, "DESDynI—a NASA mission for ecosystems, solid earth and cryosphere science," in *Proc. Int. Workshop Sci. Appl. SAR Polarimetry Polarimetric Interferom.*, Jan. 2009, pp. 26–30.
- [13] M. W. Spencer, C. Wu, and D. G. Long, "Improved resolution backscatter measurements with the seawinds pencil-beam scatterometer," *IEEE Trans. Geosci. Remote Sens.*, vol. 38, no. 1, pp. 89–104, Jan. 2000.
- [14] J. C. Curlander and R. N. McDonough, *Synthetic Aperture Radar Systems and Signal Processing*. Hoboken, NJ, USA: Wiley, 1991.
- [15] R. Ahmed, P. Siqueira, and S. Hensley, "Analyzing the uncertainty of biomass estimates from L-band radar backscatter over the Harvard and Howland forests," *IEEE Trans. Geosci. Remote Sens.*, vol. 52, no. 6, pp. 3568–3586, Jun. 2014.



Scott Hensley (SM'10) received the B.S. degrees in mathematics and physics from the University of California at Irvine, CA, USA, and the Ph.D. degree in mathematics from Stony Brook University, Stony Brook, NY, USA, where he specialized in the study of differential geometry.

He has a broad range of expertise spanning over 20 years in radar remote sensing, including the design, performance evaluation, processing and application algorithms, calibration, and data interpretation for geophysical applications in both Earth and planetary sciences, and in managing the development of complex radar interferometric systems from inception to operational platforms, including developing novel algorithms for the processing and exploitation of such systems. He has worked on most of the synthetic-aperture-radar systems developed at JPL over the past two decades, including the Magellan and Cassini radars. He was the geographic synthetic aperture radar (GeoSAR) Project Scientist, a simultaneous X-band and P-band airborne radar interferometer for mapping above and beneath the canopy that is now commercially operated by Earthdata International. He led the SRTM Interferometric Processor Development Team for a shuttle-based interferometric radar used to map the Earth's topography between 60 latitude. Recently, he began working with the Earth-based Goldstone Solar System Radar to generate topographic maps of the lunar surface. He was the Principal Investigator and is currently the Project Scientist for the NASA UAVSAR program.



Shadi Oveisgharan was born in Isfahan, Iran, in 1977. She received the B.Sc. degree from the Sharif University of Technology, Tehran, Iran, in 1999, the M.S. degree from the University of Michigan, Ann Arbor, MI, USA, in 2002, and the Ph.D. degree from Stanford University, Stanford, CA, USA, in 2007. She spent two years as a NASA Postdoctoral Fellow at the Jet Propulsion Laboratory, Pasadena, CA, USA, and joined as an employee in 2010.

Her current research interests include electromagnetic scattering theory, defining science requirements

for NASA radar remote sensing missions, and modeling interferometric observations in different environments.



Sassan Saatchi (S'85–M'88) received the B.S. and M.S. degrees in electrical engineering from the University of Illinois, Chicago, IL, USA, in 1981 and 1983, respectively, and the Ph.D. degree from George Washington University, Washington, DC, USA, in 1988. His Ph.D. thesis was on the concentration in electrophysics and modeling of wave propagation in natural media.

From 1989 to 1991, he was a Postdoctoral Fellow with the National Research Council and was with the Laboratory for Terrestrial Physics, NASA/Goddard

Space Flight Center, Greenbelt, MD, USA, working on the hydrological application of active and passive microwave remote sensing. Since April 1991, he has been with the Radar Science and Engineering Section, Jet Propulsion Laboratory, California Institute of Technology, Pasadena, CA, USA, where, as a Scientist, he is involved in developing microwave scattering and emission models for soil and vegetated surfaces and retrieval algorithms for estimating biophysical parameters from spaceborne remote sensing instruments. He has been a Principal or Coinvestigator in several interdisciplinary international projects such as First International Satellite Land Surface Climatology Project (ISLSCP) Field Experiment (FIFE), European field experiment in a desertification-threatened area (EFEDA), Magellan, The microwave aircraft experiment for hydrology (Mac-Hydro), hydrology-atmosphere pilot experiment in the Sahel (Hapex-Sahel), The Boreal ecosystem-atmosphere study (BOREAS), land-cover and land-use change (LCLUC), and large scale biosphere-atmosphere experiment in Amazonia (LBA). His present research activities include biomass and soil surface moisture estimation in different ecosystems, land-use and land-cover change, forest regeneration monitoring over tropical rain forests, and ecological modeling of species range distribution and biodiversity using remote sensing. His research interests also include wave propagation in disordered/random media and electromagnetic scattering theory. He has been involved in developing and teaching courses in the use of remote sensing for environmental problems.



Marc Simard received the B.Sc. degree from Queen's University, Kingston, Ontario, Canada, in 1992 and the M.Sc. degree in physics and the Ph.D. degree in geomatics from the Université Laval, Quebec City, Quebec, Canada, in 1994 and 1998, respectively.

He has been with the Jet Propulsion Laboratory, Pasadena, CA, USA, since 1998 and is a NASA Principal Investigator developing radar and lidar applications to measure forest canopy structure. His research generally aims at using large scale mapping of terrestrial ecosystems to improve the understanding of underlying ecological processes and their vulnerability to human activity and climate change.



Razi Ahmed (S'08–M'13) received the B.S.E.E. degree from the National University of Sciences and Technology, Islamabad, Pakistan, in 2002, and the M.S. and Ph.D. degrees in electrical and computer engineering from the University of Massachusetts, Amherst, MA, USA, in 2012.

He is currently a NASA Postdoctoral Fellow with the Jet Propulsion Laboratory, Pasadena, CA, USA. His research interests include radar remote sensing, synthetic aperture radar, interferometry and polarimetry, and its application to remote sensing of

vegetation characteristics.



Ziad Haddad received the B.A. degree in mathematics and computer science from the University of California, Los Angeles, CA, USA, in 1980 and the Ph.D. degree in mathematics from the Massachusetts Institute of Technology (MIT), Cambridge, MA, USA, in 1983.

He has taught applied mathematics at MIT, analyzed radar detection and tracking problems at MIT's Lincoln Laboratory, Lexington, MA, USA, modeled wave propagation in complex media at AT&T Bell Laboratories, taught mathematics at the University of California at San Diego, CA, USA, and pursued his research interest in nonlinear filtering and estimation. He has been with the Jet Propulsion Laboratory, Pasadena, CA, USA, since 1991. His current research interests include the development of stochastic algorithms for the retrieval of precipitation profiles and the estimation of soil parameters from remote sensing data.